Graz University of Technology

Institute of Biomechanics
Center of Biomedical Engineering
Kronesgasse 5-I
8010 Graz, Austria

Master's Thesis

Determination of the layer-specific distributed collagen fiber orientations in human thoracic and abdominal aortas and common iliac arteries

to achieve the degree of
Master of Science

Author: Georg Zeindlinger
Supervisor: Professor Gerhard A. Holzapfel
Co-Advisor: Andreas J. Schriefl, MSc

March 10th, 2011

Acknowledgment

I would like to thank Professor Gerhard A. Holzapfel for the opportunity to write this thesis at the Institute of Biomechanics.
A special thanks goes to my Co-Advisor Andreas J. Schriefl who helped me during the experiments and proofread my thesis.
Many thanks to Peter Regitnig and Mohamed Al-Effah from the Institute of Pathology, Medical University Graz, who provided the histological sections of the specimen.
I would also like to thank all co-workers, who always were eager to answer questions, if in their field of expertise.
And last but not least thanks to my family, who supported me during my whole studies at the Graz University of Technology.

Abstract

According to the reports of the World Health Organisation (WHO) cardiovascular diseases are the number one cause of death world wide. Specifically, arterial disease and degeneration are the major reasons for cardiovascular death and disability. Because these diseases are dependent on the changes of the mechanical properties of the arterial wall, it is very important to know as much as possible about the structural composition of arteries.
The human aorta is the biggest artery in the body and consists of three main parts, ascending aorta, aortic arch and descending aorta. The walls of the arteries consist of three layers, the intima, media and adventitia, where each of the layers has different physiological functions and therefore distinct mechanical properties. These were investigated by others, using, e.g., uniaxial tensile-, inflation- or planar biaxial-testing. The results showed nonlinear, anisotropic mechanical responses, indicating that the arrangement of collagen fibers is playing a crucial role in vascular mechanics.
The main focus of this study lies on the descending thoracic and abdominal aortas and the common iliac arteries. We measured location- and layer-specific collagen fiber orientations using polarization microscopy in combination with a universal rotary stage. To enhance the visibility of the collagen fibers in the polarized light, we used the well established picro-sirius-red staining method. Additionally, we measured wall thicknesses of the whole descending aorta and common iliac arteries using a video-extensometer, a micrometer gauge and a microscope.
From eleven healthy non-atherosclerotic aortas over 37.000 three-dimensional collagen fiber orientations were measured and analyzed. Our results show, that the collagen fibers of each arterial layer are distributed differently in azimuthal direction with no diversion in radial direction, meaning they are arranged in plain of the arterial wall. In most cases two fiber families symmetrically arranged around the axial and circumferential directions were found. Fibers in the media showed the most circumferential alignment, whereas in the adventitia a more axial direction of the two fiber families was observed.

Our results provide qualitative and quantitative structural data for the collagen fiber orientations of healthy non-atherosclerotic arterial walls. This data can be used directly to obtain dispersion parameters for constitutive models of arterial walls, resulting in a better physiologic modeling of the cardiovascular system.

Kurzfassung

Gemäß den Berichten der Weltgesundheitsorganisation (WHO) sind Herz-Kreislauf-Erkrankungen weltweit die häufigste Todesursache. Erkrankungen der Arterien und deren Degeneration sind eine der Hauptgründe warum es zu Herz-Kreislauf-Beschwerden, bzw. Versagen kommt. Die Erkrankungen der Arterien gehen meist mit einer Veränderung der mechanischen Eigenschaften der arteriellen Wand einher, deshalb ist es wichtig so viel wie möglich über den Aufbau von Arterien zu verstehen.
Die menschliche Aorta ist die größte Arterie im Körper. Sie besteht aus drei Hauptabschnitten, der aufsteigenden Aorta, dem Aortenbogen und der absteigenden Aorta. Die Wände von Arterien besitzen drei verschiedene Schichten, wobei jede andere physiologische Aufgaben erfüllt und sie deshalb auch unterschiedliche mechanische Eigenschaften aufweisen. Diese wurden bereits untersucht, unter anderem mittels Uniaxialen-, Inflations- oder Biaxialen-Tests. Die Ergebnisse zeigten ein nichtlineares, anisotropes Verhalten der Arterien, welches ein Hinweis ist auf die Abhängigkeit der mechanischen Eigenschaften der Blutgefäße von den Ausrichtungen der Kollagenfasern.
In dieser Studie wurde der Fokus auf die absteigende Brust- und Bauchaorta und die gemeinsame Darmbeinarterie gelegt. Wir haben die Faserorientierung mittels Polarisationsmikroskopie in Kombination mit einem Zeiss Universaldrehtisch, in Abhängigkeit von Position und Schicht, erfasst. Als kontrastverstärkenden Farbstoff für die histologischen Gewebeschnitte wurde Picro-Sirius-Rot eingesetzt, welches spezifisch an Kollagen bindet und so die Identifizierung des Kollagens einfacher gestaltet. Zusätzlich wurde noch die Wanddicke der absteigenden Aorta und der Darmbeinarterie mittels einem Video-Extensometers, einer Mikrometerschraube und einem Lichtmikroskop gemessen.
Es wurden insgesamt über 37000 Messwerte von elf gesunden nicht atherosklerotischen Aorten erfasst und ausgewertet. Aus den Ergebnissen kann gefolgert werden, dass abhängig von der Arterienschicht, die Kollagenfasern in unterschiedlichen Vorzugsrichtungen in azimuthaler Ebene angeordnet sind. Es ergab sich aber keine nennenswerte Abweichung in

radialer Richtung, d.h. die Fasern liegen plan in der arteriellen Wand. In den meisten Fällen konnten zwei achsensymmetrische Faserfamilien gefunden werden, die zueinander in einer Helix angeordnet sind. In der Media sind die Fasern nahe der Umfangrichtung und in der Adventitia am meisten in Axialerrichtung ausgerichtet.
Unsere Ergebnisse stellen qualitative und quantitative strukturelle Daten der Kollagenfaserorientierung in gesunden Arterienwänden dar. Aus ihnen können direkt Parameter für eine konstruktive Modellierung der arteriellen Wand gewonnen werden, was zu einem physiologischeren Modell des Herz-Kreislauf-Systems beitragen kann.

Contents

List of Figures

List of Tables

1 Introduction

1.1 Motivation

The World Health Organization (WHO) reports that cardiovascular diseases are the number one cause of death world wide. Arterial disease and degeneration are the major cause of cardiovascular death and disability. These degenerations are not only dependent on chemical anomalies, but can also be caused by changes in the mechanical properties of the arterial wall (O'Rourke 1995). Because of the changing mechanical behavior, the structural composition of the arteries is believed to adapt, e.g. the intima thickens when wall stresses decrease or elevate (Stary 1992), which may result in arteriosclerosis. Aneurysms might enlarge due to a stress driven growth and remodeling of the collagen increasing the risk of rapture (Humphrey and Canham 2000). Growth and remodeling of collagen is not only present in deceased arteries, but also occur naturally during the aging process as, e.g., the elastin to collagen ratio changes with age, causing a stiffening of the vessel wall known as arteriosclerosis (Ahlgren et al. 1997).
The structural composition of the arteries is different among species (Grant 1967). However, to our knowledge data on the collagen fiber orientations in healthy human aortas and common iliac arteries are not available to date.
The angles of distributed collagen fibers have significant influence on the mechanical properties of the aorta and generally on collagenous soft and hard tissues (Fung 1993, Canham et al. 1996, Holzapfel et al. 2000, Gasser et al. 2006, Holzapfel and Ogden 2010).

1.2 Collagen

Collagen is the most abundant protein in mammal soft and hard tissues and is responsible for the structural integrity (Fratzl 2008). 28 different types of collagen are known so far, however, approximately $90\,\%$ of the collagen in a human body is fibrous collagen type I. Collagen III is a second important fibrous collagen type in tissues and forms thinner fibrils

than collagen type I (Wolman and Kasten 1986).
Collagen is composed of tropocollagen molecules (triple helix) forming fibrils, which arrange to form collagen fibers (Buehler 2008). Figure 1.1 shows a schematic overview of the hierarchical features of collagen, from the molecular level up to the fiber structure.
In our study we utilize the birefringent properties of Collagen I and III to measure their fiber orientation (Section 2.4.1).

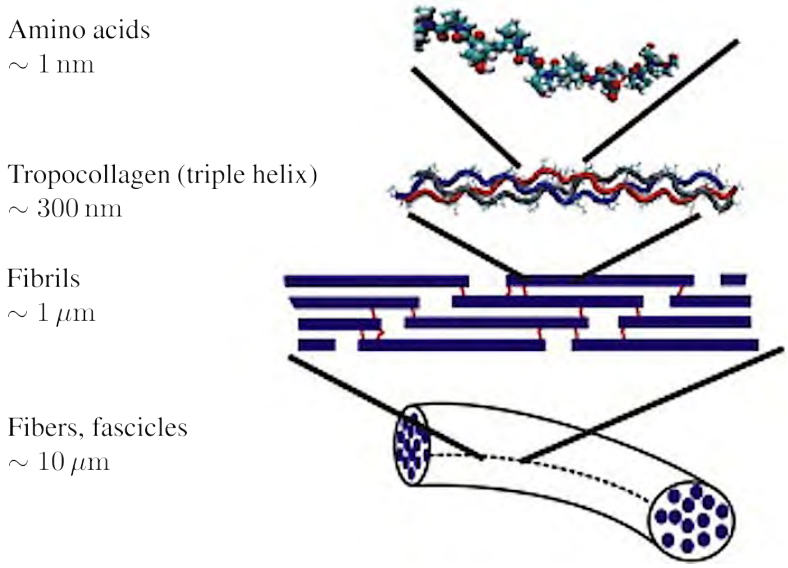

Figure 1.1: Schematic view of the hierarchical features of collagen, ranging from the amino acid sequence level at the nanoscale up to collagen fibers with lengths on the order of 10 μm (Buehler 2008).

1.3 Anatomy of the aorta

The aorta is the biggest artery of the human body and is responsible for the main blood supply. Generally arteries can be divided into elastic and muscular arteries. Elastic ones are closer to the heart, muscular ones near the periphery. However, the separation is not that strict because there are also intermediate types and the transition from elastic to muscular is a smooth one.

1.3.1 The human aorta

The human aorta is a cylindric tube and is divided into three major parts, the ascending aorta (*aorta ascendens*), the aortic arch (*arcus aortae*) and the descending aorta (*aorta descendens*) as shown in Figure 1.2. The ascending aorta starts at the aortic valve in the left ventricle of the heart and goes a few centimeters straight upwards and continues into the aortic arch. In the aortic arch are the branches to the upper parts of the body (brachiocephalic artery, common carotid artery, subclavian artery).

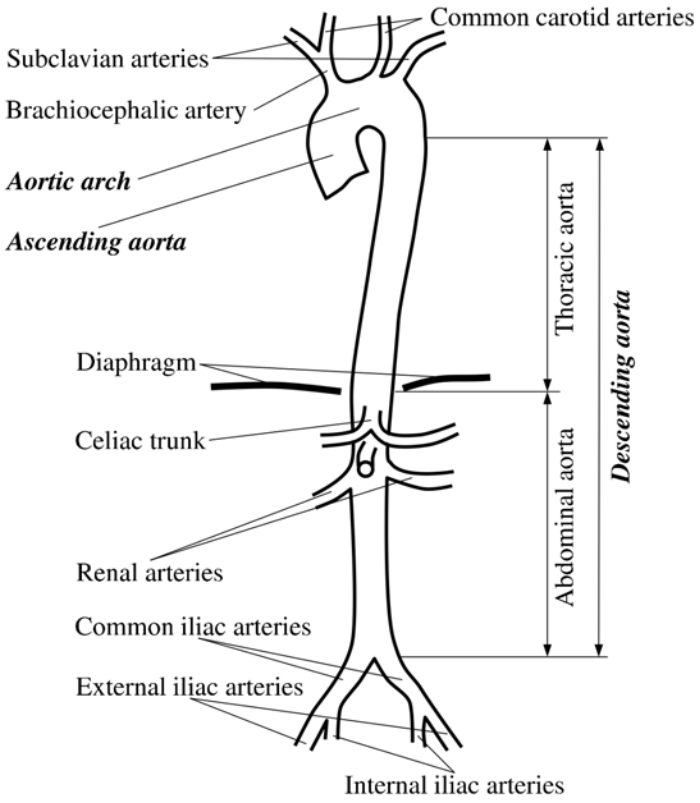

Figure 1.2: Anatomy of the human aorta and its most important parts and branches.

After the branches the descending aorta begins, which can be divided in two mayor parts, the thoracic (*aorta thoracica*) and the abdominal aorta (*aorta abdominalis*). The thoracic aorta is mostly straight with smaller branches, which supply the pericardium, intercostal space, esophagus and lung (provides blood for the lung cells, not for the oxygenation) with blood. The thoracic aorta ends at the thoracic diaphragm. From there on the aorta is called the abdominal aorta.

The main branch of the abdominal aorta is the celiac trunk which supplies the liver, stom-

ach, spleen and parts of the duodenum and the pancreas. At the end of the abdominal aorta is the bifurcation into the left and right common iliac arteries, which part again soon afterwards into the external and internal iliac arteries. Our experiments focused on the descending thoracic and abdominal aorta and the common iliac arteries (Figure 1.2).

The arterial wall

All arterial walls have three layers, the intima (*tunica intima*), media (*tunica media*) and adventitia (*tunica externa*) (Figure 1.3). Each of the three layers has a different structure, e.g., a different composition of cells, and mechanical properties. Collagen I, III and elastin are embedded into the non-fibrous, glycosaminoglycan-rich extra cellular matrix (ECM) of the arterial wall. Elastin is responsible for the elasticity and collagen for the stiffness.

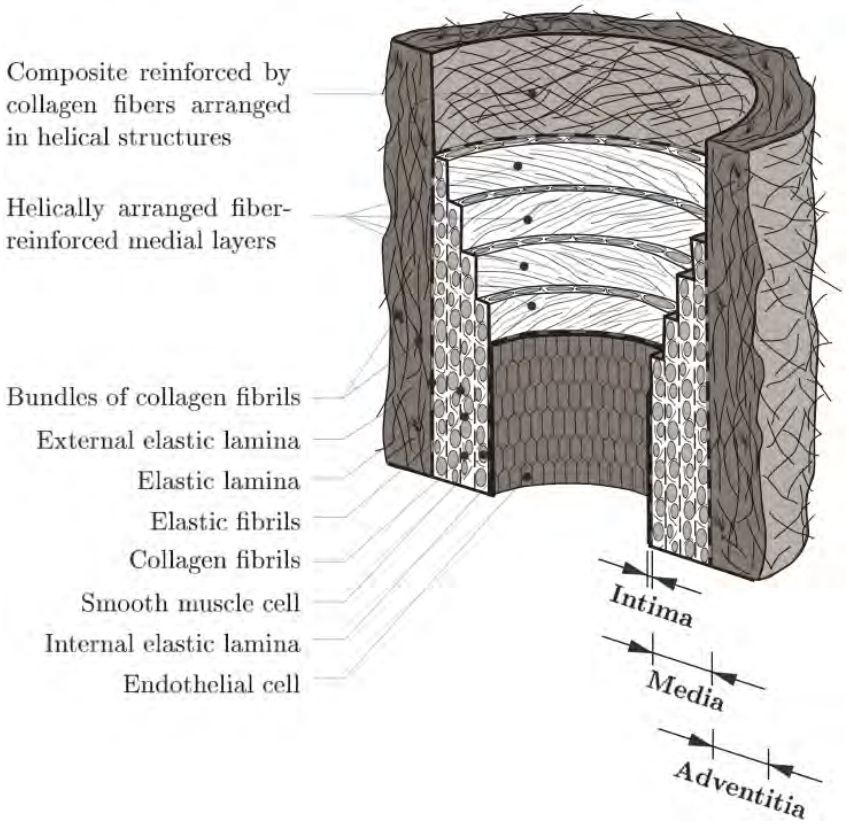

Figure 1.3: Schematic histological anatomy of a human arterial wall from Holzapfel et al. (2000).

- **Intima:** The intima is the innermost layer of the aorta. In young, healthy humans it consists of a single layer of epithelial cells at the lumen, a basal membrane (basal

lamina) and a sub-endothelial layer. The epithelial cells and the sub-endothelial layer are not one of the defining structures for the mechanical properties in young arterial walls. However, the sub-endothelial layer can alter its thickness with age or decease (Stary et al. 1992) and might then become mechanically more important (Holzapfel et al. 2000).

- **Media:** The media is the middle layer of the artery, and consists of a three-dimensional network of smooth muscle cells, elastin and collagen. The media is composed of concentrical fiber-reinforced medial layers, separated by elastic laminae. It is the structurally most important layer of the arterial wall at normal pressures (Holzapfel et al. 2000).

- **Adventitia:** The adventitia is the outer layer and consists of fibroblasts and fibrocytes (cells producing collagen and elastin) and thick collagen bundles. It is surrounded by loose connective tissue, to enable a flexible connection of the artery with the body. At elevated pressures it forms a stiff tube due to the helical arrangement of the collagen fibers, preventing the artery from over-stretching (Holzapfel et al. 2000).

1.3.2 Pig aorta

The anatomy of the pig aorta is very similar to the human aorta, which is why many studies are based on pig aortas. The major difference is the size. The human aortas used in our study were bigger in length and diameter, although the wall thickness was nearly the same. Histologically there is not much difference between the two species. The wall of the pig aorta (approximately six months old) also has three layers, but is much healthier and the layers are not as easy to differentiate as in the human aortas, who were aged 63 years on average. The intima of pig aortas we studied always consisted of one single epithelial cell layer, while a neo-intima was always present in our human samples.
Such differences make the direct comparison of data among species difficult, hence experiments with human tissue is indispensable for an improved mechanical understanding of the arterial wall (Wolinsky and Glagov 1969).

2 Methods and Materials

Coordinates and locations

For unambiguous measurements and data analysis we had to define directions and locations in our specimen and along the aortic tree.
Therefore, we defined a coordinate system where X, Y and Z are the circumferential, axial and radial directions, respectively. Generally two Eulerian angles are sufficient to be able to describe the orientation of a collagen fiber in a three-dimensional space, the azimuthal angle Φ in the X – Y plane and the elevation angle Θ in the X – Z plane. Reference or undeformed configurations are always labeled with capital letters (X, Y, Z, Φ, Θ), whereas lower case letters denote deformed configurations ($x, y, z, \varphi, \vartheta$). The coordinate system does not change its direction during the deformation (Figure 2.1).

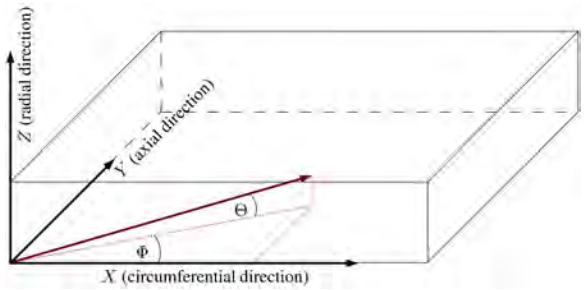

Figure 2.1: Definition of the coordinate system for measuring the orientation of a straight fiber in the arterial wall. Θ . . . elevation angle, Φ . . . azimuthal angle.

For a location-specific analysis along the aortic tree, we divided the aorta into seven parts, T1 – T3, A1 – A3 and CI, which refer to the thoracic and abdominal aorta and common iliac artery, respectively (Figure 2.2).

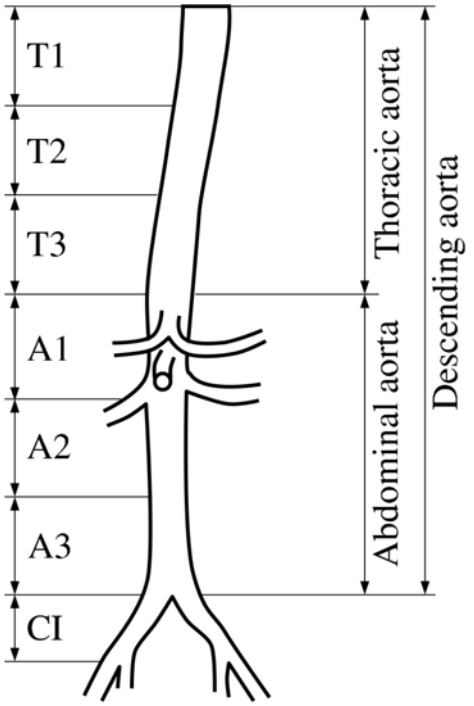

Figure 2.2: Definition of locations T1 – CI along the aortic tree.

2.1 Histological process

To obtain histological sections necessary for polarizing microscopy the following steps were performed at the Institute of Pathology, Medical University Graz, similar to those outlined in Lang 2006:

- **Dehydration:** Formalin is a hydrous fluid in contrast to paraffin which is hydrophobic. To transfer the tissue from the watery to hydrophobic stage, fluids are needed which combine with water and an organic solvent. For dehydration, the tissue undergoes different baths of alcohol. The concentration of the alcohol increases with each bath, from 50, 70, 96 to $100\,\%$ ethanol. Thus, all hydrous components (the fixing solution and tissue fluid) are chemically expelled. Also some cell components like lipids, are dissolved. Ethanol hardens and shrinks the tissue ($10\,\%$ to $15\,\%$).

- **Clearing:** After the dehydration the tissue has to be soaked in xylol (dimethylbenzol, $C_6H_4(CH_3)_2$), which combines likewise with alcohol and paraffin. Xylol makes the tissue transparent and as a organic solvent it can dissolve lipids from the tissue. It also hardens formaldehyde fixed tissue, therefore the tissue should not be left too long in xylol.

- **Infiltration:** The tissue is transferred into a bath with approximately 52 – $60\,^{\circ}\mathrm{C}$ liquefied paraffin wax. The paraffin infiltrates the voids in the tissue. The automatic tissue processor at the Institute of Pathology, Medical University Graz, Tissue-Tek®VIP®Vacuum Infiltration Processor (Sakura Finetek Europe, Alphen aan den Rijn, Netherlands), uses vacuum to speed up the infiltration process. The lower pressure aids the vaporization of the clearing fluid and the infiltration of the paraffin. By cooling to room temperature the paraffin hardens.

- **Embedding:** For the embedding process, paraffin with a higher melting point is used. The specimen is positioned into the desired orientation to obtain sections parallel to the circumferential–axial (x – y) plane (Figure 2.1). The paraffin is cooled and solidifies, therefore preserving the specimen and giving the tissue the required stiffness for the subsequent microtome slicing. The infiltration and embedment medium has to be stiffer than the stiffest structure in the tissue in order to produce thin sections with a microtome.
  The embedded tissue is cut out from the aluminum frame and now ready for the subsequent microtome slicing.

The steps "Dehydration, Clearing and Infiltration" are processed automatically with the Tissue-Tek®VIP®, which is a computer controlled tissue processor. The Embedding was performed manually. During the processing the specimen was fixed in an aluminum frame to prevent it from shrinking and warping.

Sectioning

The specimen in the paraffin block was at first cut into two parts, one to obtain planar sections (x – y plane, Figure 2.1) and the other to obtain the cross sections (x – z plane). The sections were cut with a *Microm HM 335* (Microm, Walldorf/Baden, Germany).

- **Cross sections:** From every specimen two $8\,\mu\mathrm{m}$ thick cross sections (x – z plane) were made (Figure 2.3).

- **Planar section:** To obtain planar sections (x – y plane) the following protocol was used: After the first cut a series of six $8\,\mu\mathrm{m}$ thick planar sections was made, followed by a gap of $100\,\mu\mathrm{m}$ before starting with the next six subsequent cuts. This results in a total distance of $8\,\mu\mathrm{m} \cdot 6 + 100\,\mu\mathrm{m} = 148\,\mu\mathrm{m}$ between the cut series (Figure 2.4). The number of planar sections per specimen depended on the arterial wall

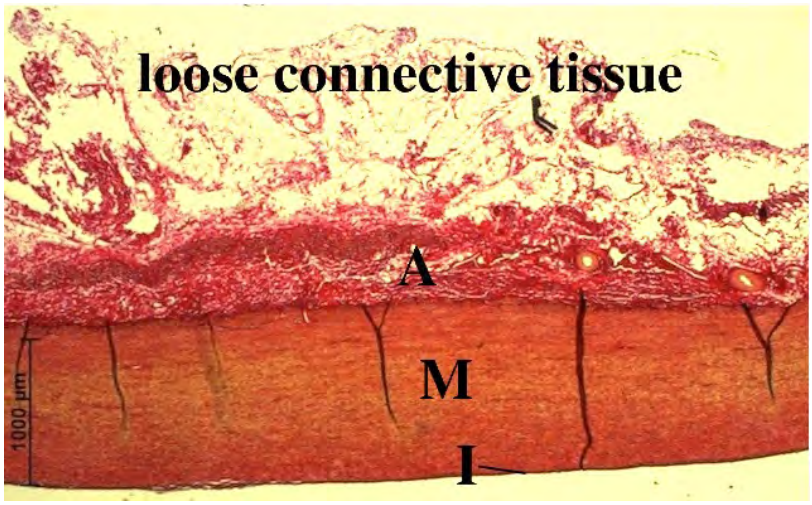

Figure 2.3: Snapshot of a histological cross section (x – z plane) from a porcine aortic wall, with clearly visible intima (I, single endothelial layer), media (M) and adventitia (A). Taken with $2.5\times$ magnification.

thickness. Only the first section of each series was stained using picro-sirius red, the other sections were used as backup if something went wrong during the sectioning or staining.

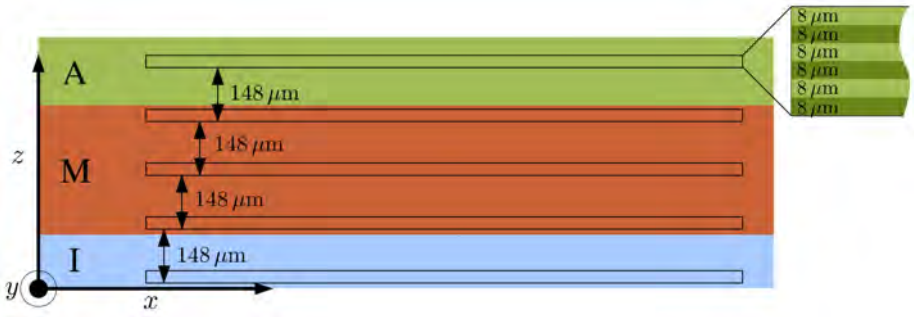

Figure 2.4: Illustration of the protocol for obtaining planar tissue sections. The number of sections varied with the specimen thickness. A . . . Adventitia, M . . . Media, I . . . Intima. Directions: x . . . circumferential, y . . . axial, z . . . radial.

Staining

After the tissue processing, slicing and placing the section onto a microscope slide, the tissue was stained. For the enhancement of the birefringence of collagen a picro-sirius red staining was used (Junqueira et al. 1979). For a standard staining process the following steps are executed (Lang 2006, Puchtler et al. 1973).
The staining process starts with warming the sections to 56 – $60\,^{\circ}\mathrm{C}$ to melt the paraffin. Then the warm glass slide is put into the clearing reagent xylol to de-wax the histological section. After the paraffin is removed, the section is rehydrated using a descending alcohol sequence ($100, 96, 70, 50\,\%$ ethanol), 1 – $2\,\mathrm{min}$ per alcohol concentration, and at last distilled water. Now the section is stained with picro-sirius red for a minimum of one hour to get a good result. Longer times do not increase the quality of the staining.
After washing with acidified water ($5\,\mathrm{ml}$ glacial acetic acid in $1\,\mathrm{l}$ water) and removing most of the water from the sections, they are dehydrated using three changes of $100\,\%$ ethanol and are cleared after the dehydration in xylol. Finally the sections are covered with a mounting medium with a refraction index approximately the same as glass slides (~ 1.53) and a thin glass coverslip. After the staining the sections are ready for the microscopic analysis.

2.2 Preliminary tests

To be able to determine a preparation protocol to produce high quality tissue samples for the histological process, we tested different methods on porcine aortas. The *in vivo* aorta in every mammal is pre-stretched in the longitudinal direction, and the blood pressure stretches the vessel in the circumferential direction.
To obtain and maintain such a pre-stretched state of the specimen we tried different methods resulting in two benefits: (i) The *in vivo* conditions of the specimens are approximated and (ii) at a loaded state the collagen fibers are straightened, which allows for a better measurement of the fiber orientation.
At first we needed to know how much the aortas are stretched *in vivo*. For the preliminary tests with pig aortas we took the data reported by Han and Fung (1995) and Guo and Kassab (2004).
Han and Fung (1995) measured the location dependent longitudinal stretch ratio of canine and porcine aortas. They used farm pigs and marked $\geq 10\,\mathrm{mm}$ sections along the aorta

using black water-resistant ink. The length of the aorta was measured *in situ* and also after the excision for the unloaded state. The longitudinal stretch ratio λ is defined as

$$\lambda = \frac{L_{situ}}{L_0}, \tag{2.1}$$

where L_{situ} is the length of the aorta *in situ*, and L_0 is the length after excision. They observed an increase of the *in vivo* stretch ratio from the aortic valve ($\lambda \sim 1.2$) to the one at the bifurcation point of the iliac arteries ($\lambda \sim 1.5$).
Guo and Kassab (2004) measured the distribution of circumferential stress and strain along pig aortas. The circumferential stretch ratios for the aortic branches, abdominal aorta and thoracic aorta were 1.4, 1.4 and 1.25, respectively.

To approximate the axial *in vivo* stretches of human aortas we used the data reported from Learoyd and Taylor (1966). In their study the subjects were divided into two groups, the 'young' group aged below 35 years, and the 'old' group aged above 35 years.
Since the arteries retract longitudinally on removal from the body, they measured the length of each segment (carotid, thoracic, abdominal, iliac, femoral) while still in the body. The amount by which a segment of the arteries shortened on removal from the body yielded in the *in situ* stretch ratios. Results for the 'old' group are shown in Table 2.1. The 'young' group showed an approximately 5 to $10\,\%$ greater retraction than the 'old' group. The retraction increases in both groups progressively towards the periphery.

Arterial location	Retraction
Upper thoracic Aorta	~ 9 – $16\,\%$
Lower thoracic Aorta	~ 11 – $19\,\%$
Abdominal Aorta	~ 15 – $22\,\%$
Common Iliac	~ 17 – $23\,\%$

Table 2.1: Longitudinal retraction of the different arterial locations of the 'old' group after the removal from the body from Learoyd and Taylor (1966).

To approximate the circumferential stretch ratio we used the data published by Labrosse et al. (2009). They experimentally measured material parameters of human aortas and compared their findings with finite element modeling to evaluate the accuracy of these models. The measured stretch ratios are not the pre-stretched values, as Learoyd and Taylor (1966) measured for the axial stretch, but the response of the vessel to a defined pressurization.

They used segments of human ascending and descending (thoracic, abdominal) aortas from eight patients with the average age of 66 ± 5 years. The inner radii, median thickness and the opening angle were measured in an unpressurized state. Under a pressure of $13.3\,\mathrm{kPa}\,(= 100\,\mathrm{mmHg})$ the circumferential and longitudinal stretch was measured. The average stretch ratios are shown in Table 2.2. The circumferential stretch ratio was evaluated at the inner radius.

Aortic location	Circumferential stretch ratio (λ_x)
Ascending	1.24 ± 0.12
Thoracic	1.31 ± 0.11
Abdominal	1.27 ± 0.11

Table 2.2: Circumferential stretch ratios at different aortic locations at an applied pressure of $13.3\,\mathrm{kPa}$ according to Labrosse et al. (2009).

2.2.1 Preliminary tests on pig aortas

Pig aortas were obtained from a local abattoir, they were approximately six months old and weighted about $100\,\mathrm{kg}$. The aortas were cleaned and the remaining fat and connective tissue was removed (Figure 2.5b). Next, the aorta was cut open axially along the branching points to avoid holes of the branches in the specimen (Figure 2.5c). The specimen was cut out using a $2 \times 2\,\mathrm{cm}$ template, the circumferential direction was marked by cutting off two corners (Figure 2.5d).

Four markers were placed in the center of the specimen to control the subsequent deformation of the specimen with the video-extensometer (Figure 2.5d). After the markers were placed the thickness was measured with a video-extensometer.

A suture based gripping method was chosen for the application of a biaxial stretch (Sun et al. 2005). Gaffs were placed with a constant distance of $5\,\mathrm{mm}$ between them and $15\,\mathrm{mm}$ to the opposite side (Figure 2.5e). Afterwards the specimen was ready to be put into a custom made biaxial stretching device (Figure 2.5f).

The first measurement of the distance between the markers was in the unloaded state (X – Y plane, Figure 2.1) to obtain the unstretched reference values of the specimen. To determine the ideal stretch state for fiber alignment, and also to reproduce the *in vivo* conditions, the stretch ratios (longitudinal and circumferential) for porcine aortas were varied within

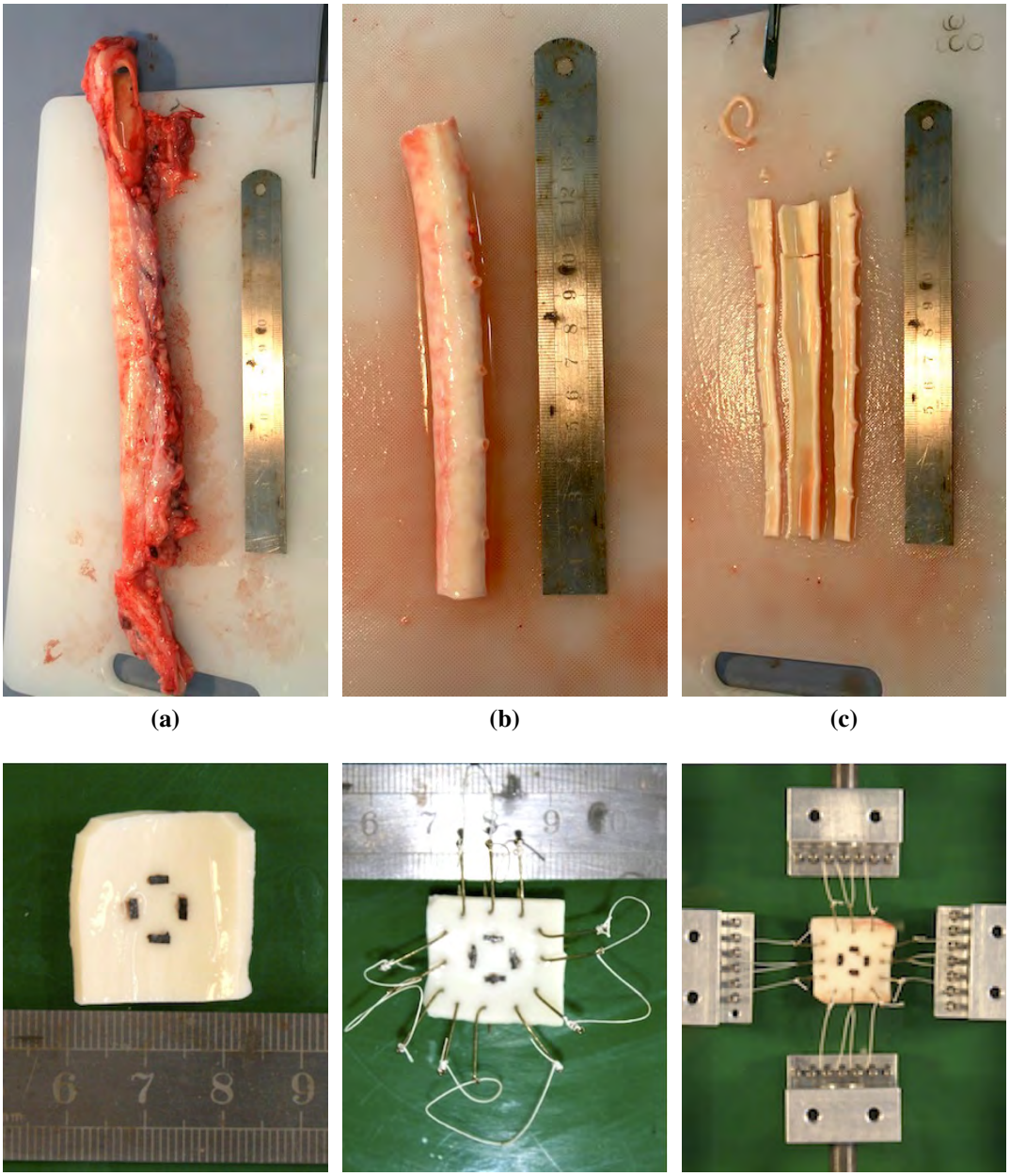

Figure 2.5: Preparation protocol: (a) Entire descending pig aorta from upper thoracic to common iliac arteries. (b) Aorta without fat and connective tissue. (c) Aorta cut open axially. (d) Cut out specimen with black markers (approximately $2 \times 2\,\mathrm{cm}$). (e) Specimen with gaffs for subsequent stretching. Gaffs are placed with a distance of $5\,\mathrm{mm}$ between each other and $15\,\mathrm{mm}$ to the opposite side. (f) Specimen placed in the stretching device.

the range reported by Guo and Kassab (2004) and Han and Fung (1995). Table 2.3 displays the different stretch ratios of all porcine specimen we tested. The histological cross sections (Figure 2.6), which are located in the x – z plane (Figure 2.1) show the effect of different stretch ratios have on the waviness of the collagen fibers.

Specimen No.	λ_x	λ_y
AS06	1.5	1.3
AS07	1.4	1.3
AS08	1.3	1.3
AS09	1.4	1.4
AS10	1.3	1.2
AS11	1.3	1.2
AS12	1.2	1.2
AS13	1.3	1.2
AS14	1.4	1.3
AS15	1.4	1.2
AS16	1.0	1.0
AS17	1.0	1.0

Table 2.3: Stretch ratios of the porcine aorta specimen in the preliminary tests, were λ_x and λ_y are the circumferential and axial stretch ratio, respectively. AS16/17 unloaded state for reference.

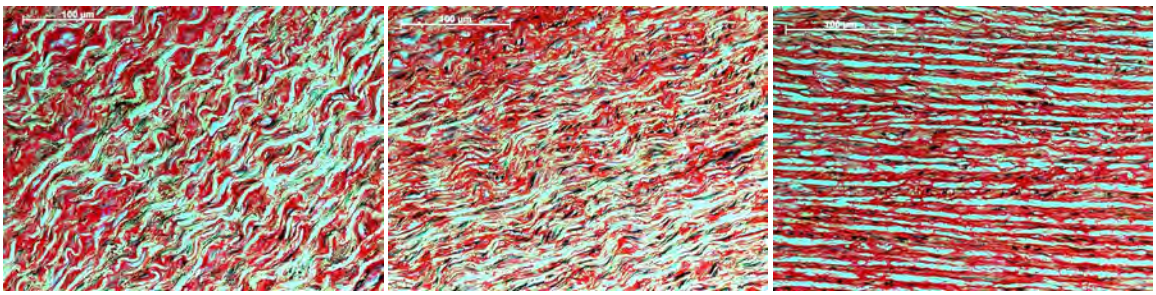

(a) **(b)** **(c)**

Figure 2.6: Different waviness of collagen fibers in a pig aorta as a function of stretch ratios. Magnification: $40\times$. (a) $\lambda_x = 1$, $\lambda_y = 1$. (b) $\lambda_x = 1.2$, $\lambda_y = 1.2$. (c) $\lambda_x = 1.4$, $\lambda_y = 1.2$.

After the specimen was stretched with the desired ratio we fixed it in $4\,\%$ phosphate buffered formaldehyde over the night for about 8 to 13 hours, while still in the stretching device. The exact recipe of the fixing solution is shown in Table 2.4. After chemical

fixation the specimen thickness was measured with a micrometer gauge (Section 2.4.2) and was put into a tube filled with the formalin for transportation to the Institute of Pathology, Medical University Graz, for the histological processing.

Substance	Formula weight	Amount	Concentration
Na_2HPO_4 (waterless)	$141.96\,\mathrm{g}\cdot\mathrm{mol}^{-1}$	$7.80\,\mathrm{g}$	$55\,\mathrm{mM}$
$NaH_2PO_4\cdot 2H_2O$	$156.01\,\mathrm{g}\cdot\mathrm{mol}^{-1}$	$1.87\,\mathrm{g}$	$12\,\mathrm{mM}$
Dissolving in H_2O, fill with H_2O		ad $900\,\mathrm{ml}$	
Formaldehyde 36 – $40\,\%$		$100\,\mathrm{ml}$	$\sim 4\,\%$

Table 2.4: Recipe of the $4\,\%$ phosphate buffered formaldehyde solution ($pH\sim 7.4$).

2.2.2 Preliminary tests on a human aorta

With the experience and data collected during the preliminary testing on pig aortas, we received ethical approval by the Ethics Committee of the Medical University Graz for studies on human tissues (Ethics Committee number: 21-288 ex 09/10).
A Human aorta extracted from a 55 year old female was provided from the pathology department. To test our preparation protocol from pig aortas on human tissue we used the stretch ratios $\lambda_x = 1.2$ (circumferential) and $\lambda_y = 1.1$ (longitudinal) for all specimens.
The fixation was always performed in the stretching device with phosphate buffered formaldehyde. The stretched human specimen tended to warp during the preparation process. To prevent the warping after the fixation in formalin, the following methods were tested: The specimen was

(a) left in the stretched state in the stretching device. All histological preparations were performed with the specimen in the stretching device,

(b) mounted in a smaller aluminum frame and fixed with surgical-sewing strand (Figure 2.7),

(c) put between glass plates.

The stretching device and the aluminum frame stopped the specimen from warping and kept it from changing its stretch values during the subsequent alcohol baths and paraffin embedment. The only problem with the stretching device was that it is an expensive prototype and due to its size difficult to handle during histological processing. Therefore the

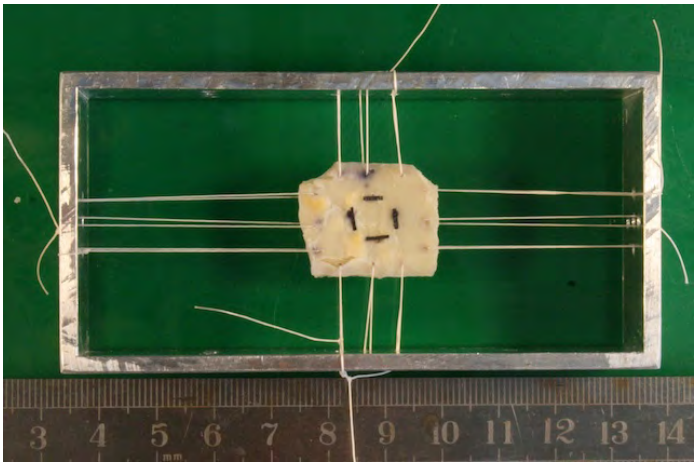

Figure 2.7: Mounted specimen in an aluminum frame using surgical sewing material to prevent shrinking during histological preparation process.

aluminum frame was the best solution to prevent the warping of the specimen during the histological process. It was easy to build and the material was cheap enough to obtain enough frames to prepare up to 20 specimen simultaneously if needed.
For most of the specimen our applied stretch ratios of $\lambda_x = 1.2$ and $\lambda_y = 1.1$ were too low, resulting in still wavy collagen fibers in younger aortas. Therefore, we set our desired stretch ratio to $\lambda_x = 1.25$ and $\lambda_x = 1.15$. However, in some cases we stopped stretching the specimen before it would be damaged, even if the desired stretch ratio was not reached.

2.3 Sample preparation

During the curse of nine month the institute of pathology, Medical University Graz, provided eleven aortas from deceased patients, six female (48 – 91 years) and five male (43 – 83 years), with an average age of 63 years. The specimen were cut out after a few hours after death and were then placed in phosphate buffered saline (PBS, the recipe is displayed in Table 2.5). The average duration of the specimen in the PBS solution until the fixation in formalin was approximately 24 hours. We tried to harvest seven specimen per aorta, one from each location, T1 – T3, A1 – A3 and CI. Every specimen had a fixation time of approximately 8 hours.
For the fixation a $4\,\%$ formaldehyde solution in phosphate buffer with a pH of ~ 7.4 was used (Table 2.4). Formaldehyde is a gas in hydrous solution, available in concentrations of 35 – $40\,\%$.

Substance	Formula weight	Amount
$NaH_2PO_4 \cdot 2H_2O$	$178.01\,\mathrm{g} \cdot \mathrm{mol}^{-1}$	$1.44\,\mathrm{g}$
KH_2PO_4	$136.09\,\mathrm{g} \cdot \mathrm{mol}^{-1}$	$0.24\,\mathrm{g}$
KCl	$74.55\,\mathrm{g} \cdot \mathrm{mol}^{-1}$	$0.2\,\mathrm{g}$
$NaCl$	$58.44\,\mathrm{g} \cdot \mathrm{mol}^{-1}$	$8\,\mathrm{g}$
Dissolving in H_2O dest.		$1000\,\mathrm{ml}$

Table 2.5: Phosphate buffered saline (PBS, $pH \sim 7.4$).

2.3.1 Preparation protocol

The final sample preparation method for human aortas included all previously mentioned procedures. The following list gives a summary of all the single steps of the preparation protocol in chronological order:

1. Clean aorta from blood, surrounding tissue and parts not needed (e.g., aortic arch, most branchings).
2. Separate, thoracic, abdominal aorta and common iliac arteries.
3. Cut open each segment in axial direction.
4. Cut out the specimen using a $2 \times 2\,\mathrm{cm}$ template and mark the circumferential direction by cutting two corners of one circumferential edge. Take a note from which part of the vessel the specimen was taken (Figure 1.2). Place the specimen in PBS (Table 2.5).
5. Measure the total thickness of the arterial wall with a video-extensometer, performed on a part of the arterial wall extracted directly next to the specimen.
6. Place the markers and hooks (gaffs) at the edges of the specimen and mount specimen in the stretching device.
7. Measure sample dimensions in the unloaded configuration with video-extensometer and try to stretch the specimen in circumferential and axial direction with a ratio of $\lambda_x = 1.25$ and $\lambda_y = 1.15$, respectively. Measure the stretched dimensions.
8. Fixation in $4\,\%$ phosphate buffered formaldehyde for approximately eight hours.
9. Measurement of the total specimen thickness with a micrometer gauge.

10. Sew specimen into aluminum frame and deposit it back in the $4\,\%$ formaldehyde.

Aortas with too much plaque or calcifications were not processed. Also not every specimen could be stretched to the desired ratio, mostly the older ones were stiffer and the hooks tended to wrench out if stretched too much, so we stopped before the specimen took any damage. For the detailed stretch ratios of every specimen see Table 2.6. On average $\lambda_{x,\mathrm{T,A}} = 1.201$ and $\lambda_{y,\mathrm{T,A}} = 1.125$ for thoracic and abdominal aorta and $\lambda_{x,\mathrm{CI}} = 1.19$ and $\lambda_{y,\mathrm{CI}} = 1.112$ for common iliac artery.

Aorta No.	**Sample**	**T**	**A**	**CI**	$\lambda_{x,\mathrm{T,A}}$	$\lambda_{y,\mathrm{T,A}}$	$\lambda_{x,\mathrm{CI}}$	$\lambda_{y,\mathrm{CI}}$
1	AS28	X			1.212	1.107		
	AS29	X			1.252	1.155		
	AS30		X		1.189	1.140		
	AS31		X		1.096	1.053		
	AS32			X			1.199	1.103
2	AS34	X			1.250	1.150		
	AS35	X			1.260	1.152		
	AS36	X			1.250	1.150		
	AS37		X		1.247	1.165		
	AS38	X			1.250	1.150		
3	AS39	X			1.115	1.051		
	AS40	X			1.160	1.055		
	AS41		X		1.092	1.075		
	AS42		X		1.101	1.066		
	AS43			X			1.206	1.104
4	AS44	X			1.258	1.155		
4	AS45	X			1.245	1.142		
	AS46	X			1.169	1.095		
	AS47	X			1.130	1.085		
	AS48			X			1.111	1.070
5	AS49	X			1.247	1.151		
	AS50	X			1.273	1.135		
	AS51		X		1.252	1.163		
	AS52	X			1.237	1.146		
	AS53			X			1.130	1.099
6	AS54	X			1.235	1.126		

Continued on next page

Aorta No.	Sample	T	A	CI	$\lambda_{x,\mathrm{T,A}}$	$\lambda_{y,\mathrm{T,A}}$	$\lambda_{x,\mathrm{CI}}$	$\lambda_{y,\mathrm{CI}}$
	AS55		X		1.222	1.137		
	AS56		X		1.063	1.048		
	AS57	X			1.248	1.065		
7	AS58		X		1.091	1.135		
	AS59		X		1.064	1.136		
	AS60	X			1.132	1.122		
	AS61	X			1.163	1.138		
8	AS62			X			1.182	1.106
	AS63		X		1.269	1.153		
	AS64		X		1.253	1.177		
	AS65	X			1.275	1.174		
	AS66	X			1.257	1.156		
9	AS67			X			1.197	1.108
	AS68		X		1.259	1.163		
10	AS69			X			1.253	1.167
	AS70			X			1.215	1.138
	AS71		X		1.268	1.158		
	AS72		X		1.264	1.149		
10	AS73		X		1.258	1.152		
11	AS74			X			1.219	1.110
	AS75			X			1.192	1.111
	AS76		X		1.153	1.086		
	AS77		X		1.162	1.107		
	AS78		X		1.158	1.107		
	AS79		X		1.182	1.112		
Average					1.201	1.125	1.190	1.112
SD					0.067	0.038	0.042	0.025
Σ		**21**	**20**	**10**				

Table 2.6: Applied stretch ratios from all eleven subjects. T...thoracic aorta, A...abdominal aorta and CI...common iliac artery, as specified in Figure 2.2.

2.4 Methods of measurement

We determined the three dimensional distribution of collagen fibers, the total aortic and arterial wall thicknesses and the thicknesses of the individual layers (intima, media, adventitia) of the vessel. In the following sections are detailed descriptions of the methods we used to obtain the reported data.

2.4.1 Angle measurements

The measurements of the collagen fiber angles were performed with the three-axial Zeiss Universal Rotary Stage UD 124, using it with the microscope Zeiss Axio Scope.A1 (Carl Zeiss MicroImaging, Göttingen, Germany). The angles were measured directly with the microscope and from snapshots made with the 5-megapixel camera AxioCam MRc5 (Carl Zeiss MicroImaging, Göttingen, Germany) mounted on the microscope. For the measurements with the microscope linear polarized light was used to utilize the birefringent properties of the collagen fibers (Junqueira et al. 1979, Wolman and Kasten 1986, Canham et al. 1996).

Polarized light microscopy

White light consists of many independent linear polarized waves, which are uniformly distributed in every direction. To polarize white light a polarizer needs to be mounted into the optical pathway, allowing only light waves in one direction to pass. It is essential to use a second polarizer (called analyzer) and it is rotated $90°$ in respect to the first polarizer. If no birefringent material (which can change the direction of the polarized light) is between the two polarizers, the analyzer can be used to measure the preferred direction of the polarizer at the point of extinction. In our hardware configuration the polarizer transmission azimuth was $0°$, which gives a position of extinction for the analyzer at $90°$.
In optical anisotropic (birefringent) materials, such as crystals (e.g., calcite) or polymers (e.g., collagen), the refraction is dependent of the direction on the incident light. If a birefringent specimen is placed between the polarizer and analyzer, the linear polarized light splits into two wave components, which are orthogonal with respect to each other. They are called the ordinary and extraordinary ray (2.8). The refractive indices n for the ordinary ray and the extraordinary ray are constant for any direction and dependent on the direction, respectively. Hence the velocities of the two wave components are different ($v = {}^{c}/_{n}$) and

this results in a phase-shift of the rays after exiting the specimen. When the rays pass through the analyzer, the components out of phase are recombined causing constructive and destructive interference. As a result the birefringent material becomes visible in the ocular with a direction dependent brightness. The direction in which the ordinary and extraordinary ray overlap and the ray of the transmitted light suffers no birefringence, is called the optical axis.

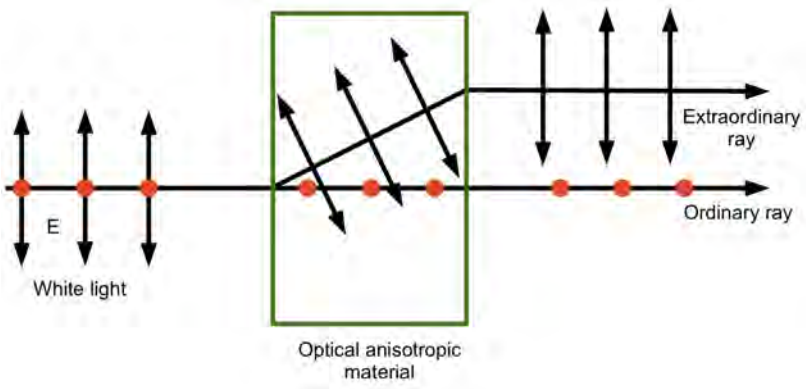

Figure 2.8: Light ray splitting into two orthogonally components (extraordinary and ordinary) in an optical anisotropic material (e.g., calcite crystal).

How to use these effects for the measurement of the collagen fiber distribution with a polarized light microscope is explained in the following with the help of an anisotropic crystal (Figure 2.9).

The polarizer and the analyzer are placed in an East-West and North-South direction, respectively. This means the polarizer and analyzer are orthogonal (crossed polarizers) to each other and no light comes through the analyzer if no specimen is in the optical path.

The specimen is assumed to be a birefringent (optical anisotropic) crystal with the optical axis oriented parallel to the longer axis. It is put between the polarizer and analyzer of the microscope, so that the optical axis of the crystal is orthogonal to the optical axis of the microscope. The crystal can also be rotated around the optical axis of the microscope with a rotary stage to change the direction of the optical axis (Figure 2.9).

If the orientation of the crystal optical axis is parallel to the angle of the polarizer (2.9a), the incident polarized light is not refracted, and therefore no split into the ordinary and extraordinary wave component occurs. The light is vibrating in a plane with the same direction as the polarizer, and no light can be transmitted through the analyzer. Therefore the crystal acts like an optical isotropic material and appears dark and is not clearly distinguishable from the background, this direction is called the point of extinction and is an important

reference point for the fiber orientation measurements. Extinction appears always when the optical axis of the crystal is parallel (Figure 2.9a) or orthogonal (Figure 2.9d) with the polarizer.

As the angle α of the optical axis is increased (Figure 2.9b), the polarized light is separated into ordinary and extraordinary wave components which are orthogonal and phase-shifted to each other (Figure 2.8). After passing the analyzer, components from both waves are filtered in the same direction and therefore can combine with constructive or destructive interference. This results in an increased brightness of the crystal. The point of maximum brightness is reached at an angle $\alpha = 45°$ (Figure 2.9c). If rotated above $\alpha = 45°$, the brightness starts to decrease until $\alpha = 90°$ where is also a point of extinction.

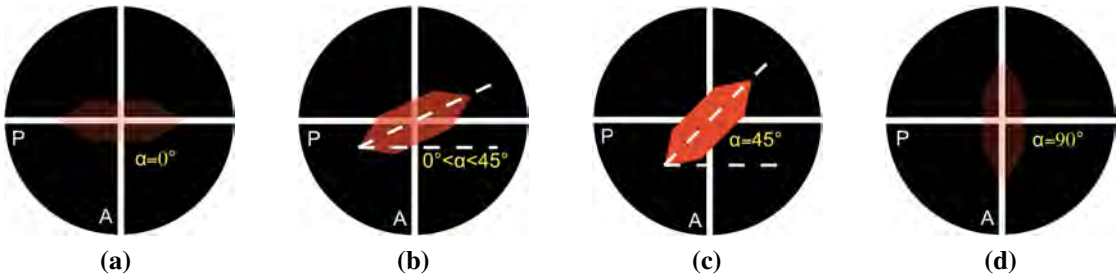

(a) **(b)** **(c)** **(d)**

Figure 2.9: Birefringent crystal in polarized light: (a) Point of extinction, crystal length (optical) axis parallel to polarizer. (b) Brightness increases with the angle. (c) Maximum brightness of the specimen at an angle $\alpha = 45°$. (d) Point of extinction, crystal length (optical) axis orthogonal to polarizer. Adopted from Landuyt (2006).

If two birefringent crystals with different orientations are placed in the microscope stage, both have the same brightness, at an orthogonal polarizer configuration, if they are symmetrically arranged around P or A (Figure 2.10a). The brightness of the single crystals depends on the position of the analyzer. Rotating the analyzer slightly into the direction of one crystal it appears brighter, the brightness of the other crystal is decreased (Figure 2.10b, 2.10c). We used this effect to take snapshots from the different collagen fiber layers which were oriented in different directions.

Birefringence of collagen I & III

Collagen I possesses (i) a positive intrinsic birefringence, meaning that the velocity of the incident light is dependent on different chemical groups in ordered configurations (like in a crystal) and (ii) form birefringence, e.g., in rod-like or plate-like bodies in a medium. If the refraction index of the embedding medium equals the one of the rod-like bodies the

(a) **(b)** **(c)**

Figure 2.10: Two birefringent crystals with different orientation in polarized light: (a) Analyzer at $90°$, both crystals appear in the same brightness. (b) and (c) The brightness of the crystal which is in the same direction as the analyzer increases, the other decreases.

effect of form birefringence can be reversed (Wolman and Kasten 1986). Positive birefringence implies that the refraction index of the extraordinary ray n_{eo} is bigger than the one of the ordinary ray (n_{o}). Stained with pirco-sirius red the positive birefringence is enhanced (Junqueira et al. 1982). Collagen III has a weak negative intrinsic and a positive form birefringence (Wolman and Kasten 1986). The refractive index of collagen was measured by Yarker et al. (1983) and lies between 1.46 and 1.55. Due to the birefringence the orientation of the collagen fibers in arterial tissue can be obtained using polarized light microscopy in combination with a universal rotary stage.

Universal rotary stage

The Zeiss Universal Rotary Stage UD 124 has three axes, which can be used to measure the three dimensional orientation of an optical anisotropic material. The universal stage can be rotated around or tilted in two axis against the optical axis of the microscope (Figure 2.11). It is often used in geology to analyze the orientation of crystals and crystalline fabrics. It consists of two glass hemispheres with a refraction index close to the one of collagen. With our microscopic hardware configuration, the refraction index can be varied between $n = 1.648$, $n = 1.556$ and $n = 1.516$. We chose the 1.516 because the refraction index of collagen was measured to be between 1.46 and 1.55 by Yarker et al. (1983).
Smith et al. (1981) and Canham et al. (1996) reported that an immersion fluid (immersion oil $n = 1.515$, Glycerol $n = 1.47$) was always used to coat the inner surfaces of the two hemispheres of the universal rotary stage. This was done to approximate the refractive index of collagen and to minimize the internal reflections, and is also mentioned in the instruction manual for the Zeiss Universal Rotary Stage UD 124. Therefore an immersion

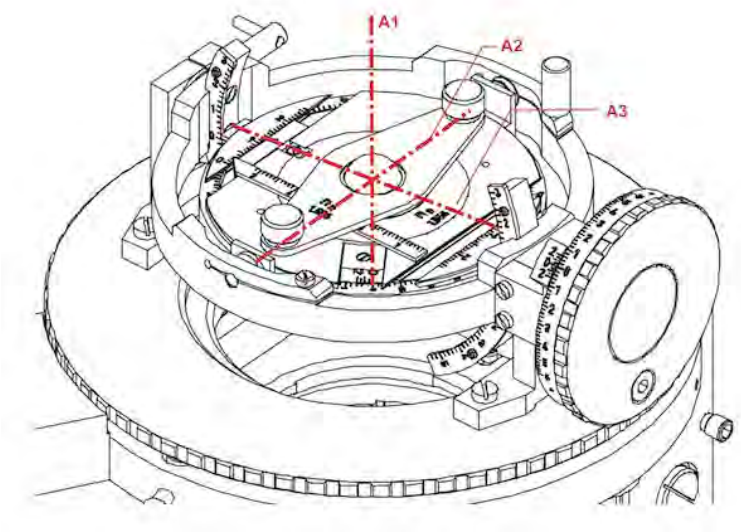

Figure 2.11: Universal Rotary Stage UD 124. A1 . . . rotation axis around the optical axis of the microscope. A2 . . . inner tilt axis. A3 . . . outer tilt axis (Picture taken from the manual).

oil with a refractive index of $n = 1.508 - 1.525$ at $20\,^{\circ}\mathrm{C}$ was used.

Measurement procedure

After placing the stained histological section into the universal stage, the main task was to find an area, which was not much affected by histological artifacts like fractions, dirt inclusions or others. This was performed with a small magnification objective ($2.5\times$). The area of interest was than centered in the optical axis of the microscope. After the centering the reference angle was measured, defining the circumferential direction, which was needed to be able to calculate the deviation of the angles from the circumferential direction described by the azimuthal angle φ (Figure 2.1). For most measurements a $20\times$ magnification objective was used, sometimes the main fiber direction was better visible with a $10\times$ magnification. At all times the polarizer and analyzer were preset at 90° with respect to each other, so that only birefringent elements of the tissue were visible.
From each section 50 azimuthal angles were measured from five different regions of the sample, at the position with the lowest brightness of the collagen bundles (point of extinction, Figure 2.12).
The elevation angle ϑ could not be measured with the universal stage, because our hardware configuration did not allow us to see the changes in the light intensity for small changes in

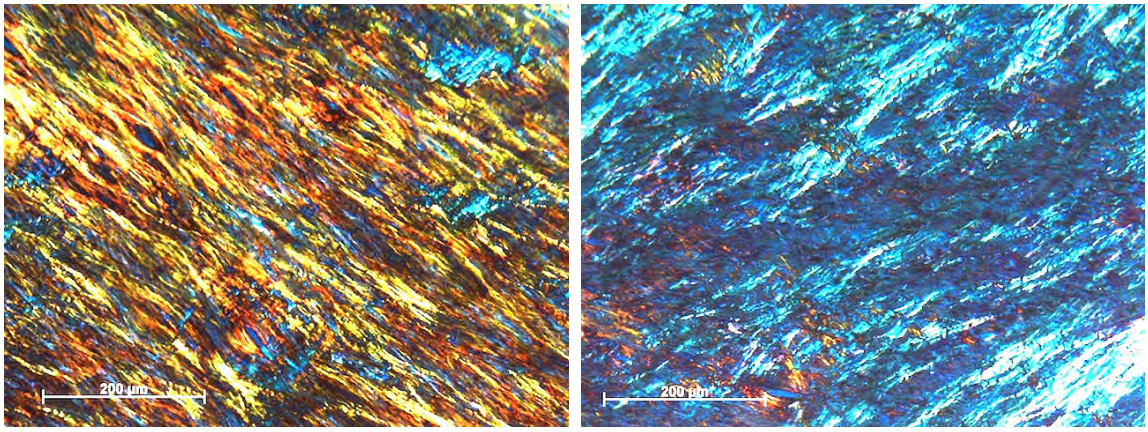

(a) **(b)**

Figure 2.12: Representative images of collagen fiber orientations in the media: (a) Arbitrary angle φ of the universal stage, high brightness of the fibers, two fiber families are visible. (b) Point of extinction for one fiber family.

ϑ. Therefore we used images of cross sections, rotated $45°$ with respect to circumferential direction for maximum brightness of the collagen fibers, to measure this angle (Figure 2.13).

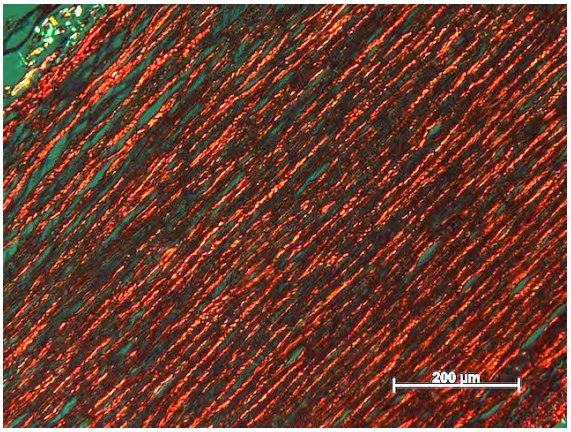

Figure 2.13: Representative image of collagen fibers lying in plane ($x - y$ plane) of the arterial wall (elevation angle $\vartheta \sim 0°$). Picture taken form a thoracic media and rotated $45°$ with respect to the circumferential direction for maximum brightness of the collagen fibers.

Besides collagen fiber angle measurements with the universal stage, four snapshots of every planar section were made with a $10\times$ magnification, while in the universal stage. The pictures were taken in circumferential direction and the analyzer was slightly rotated towards each main fiber direction to enhance their brightness (Figures 2.14a, 2.14b). To carry out

the angle measurements the software *Zeiss AxioVision 4* was used. These measurements had to be performed with care, because all fiber directions had to be measured with an equal weighting, so these measurements would not falsify our data. And in the case of the intima due to extinction some directions could not be seen if the specimen was aligned in circumferential direction. Therefore, additional snaps were taken at $45°$ and rotated with a picture manipulation program into circumference direction, to be able to measure fibers aligned in axial and circumferential direction (Figures 2.14c, 2.14d). This was only nec-

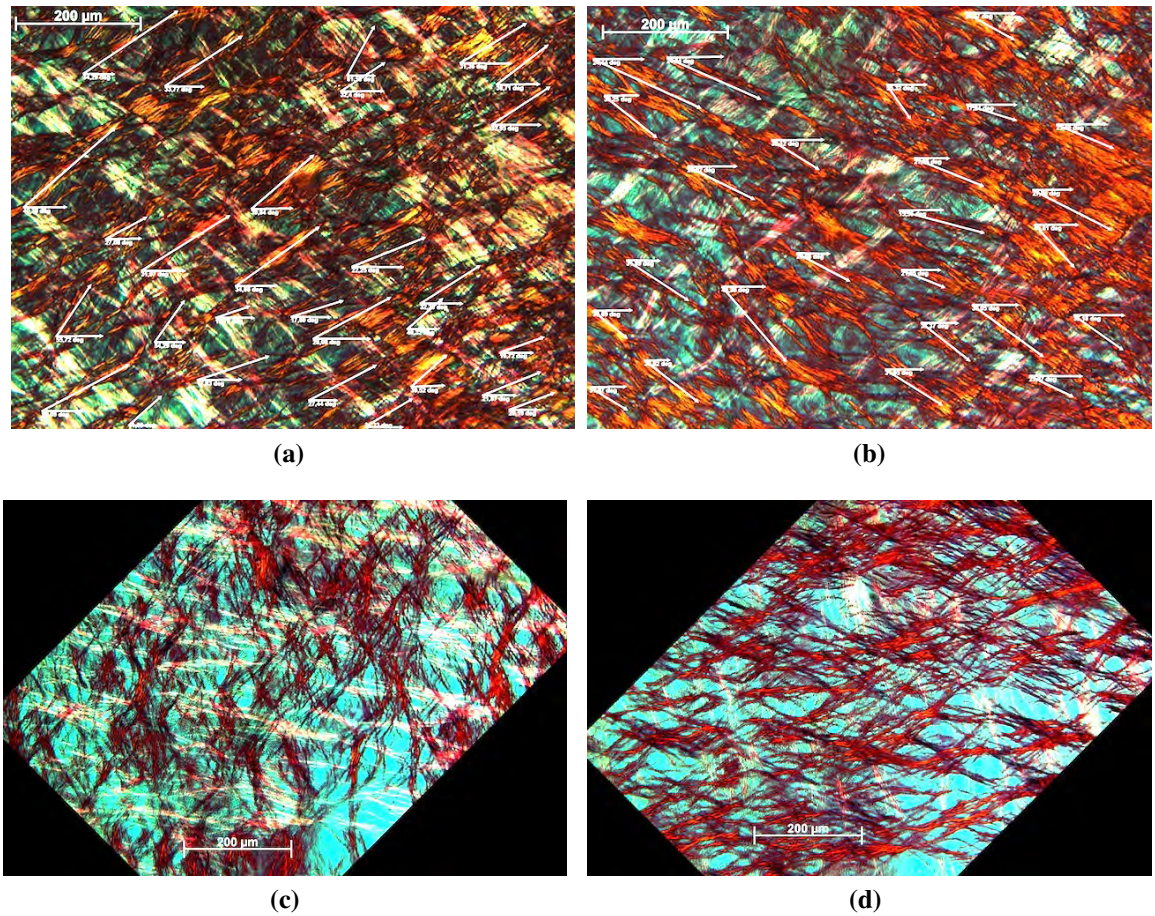

(a) **(b)**

(c) **(d)**

Figure 2.14: Four collagen fiber families in the intima: angles are measured using *AxioVision 4*: (a) First fiber family. Analyzer at $80°$ in respect to polarizer. (b) Second fiber family. Analyzer at $100°$ in respect to polarizer. (c) Third fiber family in axial direction. (d) Fourth fiber family in circumferential direction.

essary for the intima, where fiber families in the circumferential and axial direction were present.

2.4.2 Wall thickness measurements

In addition to the measurement of the orientations of collagen fibers, arterial wall thicknesses were measured. We used three different measurement methods: (i) video-extensometer, (ii) micrometer screw gauge and (iii) a microscope. With the video-extensometer and micrometer gauge we obtained the total wall thickness, with the microscope we also measured layer-specific thicknesses.

Video-extensometer

To measure the unloaded and chemically unfixed configuration a video- extensometer was used (Figure 2.15a). The calibration was performed with a $1\,\mathrm{mm}$ thick glass slide (Figure 2.15b). The edge of the glass slide was painted black with a permanent marker and the background was white, so that the software could find the boundaries of the glass slide. For the measurements of the tissue the background was changed to black to make the bright arterial wall visible (Figure 2.15c).
For the thickness measurements tissue stripes were used with approximately $20 \times 3\,\mathrm{mm}$ length and width, respectively. If the whole specimen ($20 \times 20\,\mathrm{mm}$) would be used measurement errors can be introduced, because the unfixed aorta tends to warp, which can cause the cross-section on screen to appear bigger than it really is. The layers of the aorta were not separated like, e.g., Holzapfel et al. (2007) did, instead the total wall thickness was measured using the video-extensometer. The layer-specific thicknesses were obtained using the histological cross-sections under the microscope.

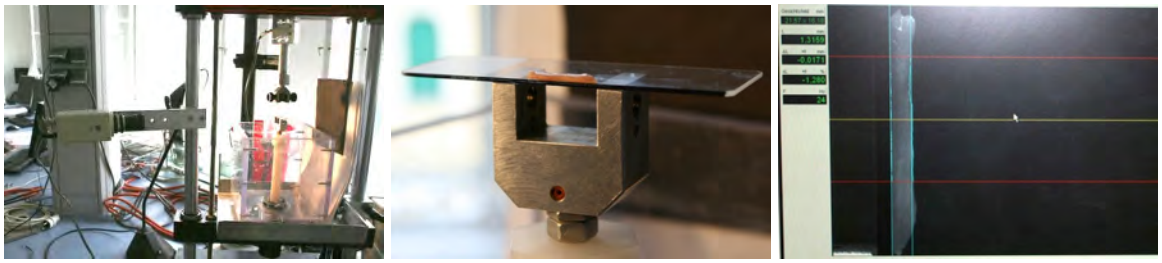

(a) **(b)** **(c)**

Figure 2.15: Measurement of the arterial wall thicknesses using a video-extensometer: (a) Mounted camera on the left. (b) Sample of the aortic wall placed on a $1\,\mathrm{mm}$ thick glass slide. (c) Cross section of the arterial wall displayed on screen, rotated $90°$.

Micrometer gauge

For these measurements an outside micrometer was used. The measurements were performed on specimens after the controlled deformation and fixation in $4\,\%$ phosphate buffered formaldehyde. Although the tissue is chemically fixed, it still can be deformed if the micrometer is fit too tight. If applied too loose, measured wall thicknesses appear to be bigger than they are, which makes the measurement challenging. This is generally the case for measurements on soft tissue with contact methods (Lee and Langdon 1996, Humphrey 2002).

Microscope

The thickness measurements with the microscope were performed (after the histological processing) using the standard configuration of the microscope (without the universal rotary stage and polarized light). The length scale was calibrated for each objective of the microscope using a stage micrometer from Zeiss with a reticle divided in $10\,\mu\mathrm{m}$ steps.
Two snapshots were taken of each layer (intima, media and adventitia) and the thickness was measured on approximately 20 locations on each snapshot using the *Zeiss AxioVision 4* software (Figure 2.16).

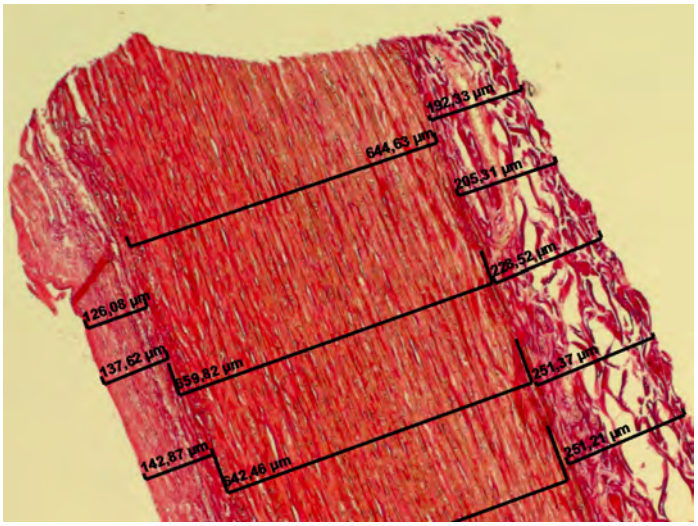

Figure 2.16: Representative image of layer-specific thickness measurements of the arterial wall.

To obtain the total wall thickness the mean values from each of the three layers were added, $x_\mathrm{t} = \bar{x}_\mathrm{I} + \bar{x}_\mathrm{M} + \bar{x}_\mathrm{A}$. The total standard deviation was calculated using $SD_\mathrm{t} = \sqrt{\sum_{i=1}^{3} SD_i^2}$

with the layer specific standard deviation $SD_i = \sqrt{\frac{1}{n-1}\sum_{j=1}^{n}(x_j - \bar{x})^2}$, were n is the number of measurements, $\bar{x}$ is the arithmetic mean and x_j are the measured values.
The measurements of the adventitia were very challenging, because often it tends to detach itself from the media during the histological slicing (Figure 2.17).

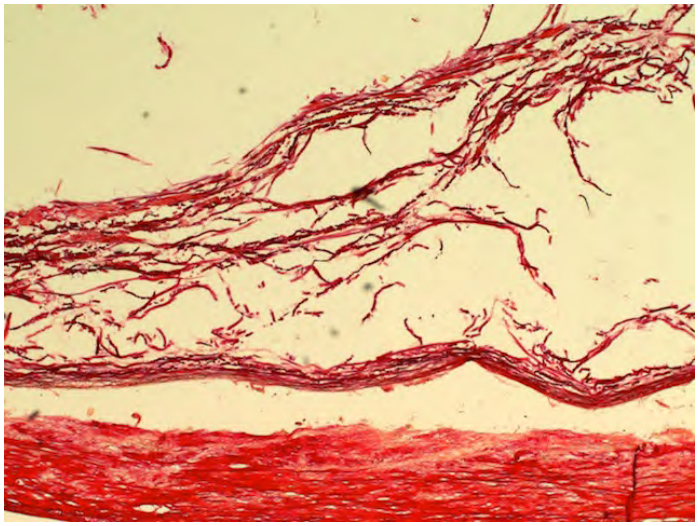

Figure 2.17: Histological cross section of the arterial wall with detaching adventitia.

The total wall thicknesses were compared with the values measured with the micrometer gauge, see Section 3.2 for results.

2.5 Continuum mechanics

We measured the angles of the collagen fibers in a stretched state. To be able to use our data in a constitutive model the angles need to be in transformed into the reference, undeformed state. This can be accomplished by using a deformation gradient. The constitutive models by Holzapfel et al. (2000) and Gasser et al. (2006) is the basis for the following sections. Also some fundamental information should be given on the subject of continuum (bio-)mechanics (Athanasiou and Natoli 2009, Holzapfel 2000).

The continuum theory introduces a way to describe a material on a macroscopic scale without paying attention to the microscopic, molecular structure of the matter. This makes it easier to describe relationships between phenomena, assuming that the matter is indefinitely divisible.

Continuum mechanics describes the response of matter (solids, liquids, gases) if forces are applied. Holzapfel (2000) divided the description of continuum mechanics into three parts:

(i) the study of motion and deformation (kinematics),

(ii) the study of stress in a continuum (concept of stress), and

(iii) the mathematical description of the fundamental laws of physics governing the motion of a continuum (balance principles).

Constitutive relationships describe an idealized material. Our assumption is that the arterial wall is an incompressible hyper-elastic solid, thus the deformed configuration can be transformed to the unloaded reference configuration with the concept of the deformation gradient.

2.5.1 Kinematics of a continuum (motion)

Kinematics describes the motion, change of position and change of a configuration over time of a continuum (solid) body. There are two different ways to calculate a motion, the Lagrangian and the Eulerian method. The later is also called the spatial description and analyzes what happens at every fixed point in space. It is used to describe the instantaneous motion and its evolution in time in respect to a specific point of interest.
In the Lagrangian (material) description the motion of every individual particle in the material is observed and therefore we get a trajectory for each individual particle. We assume that a body $\mathcal{B}$ has a continuous distribution of matter in space and time and is a composition of particles P ($P \in \mathcal{B}$).
In the following description the reference or undeformed configuration ($t = 0$) is addressed with capital letters, whereas the configuration at a time t is addressed with lower case letters.
Consider the body $\mathcal{B}$ occupies, at any given time, a region Ω in three-dimensional Euclidean space, where the position of any individual particle can be described by a vector from a fixed frame $\mathcal{O}$, with orthonormal basis vectors $\mathbf{e}_a, a = 1, 2, 3$ (Figure 2.18). Ω_0 and $\mathbf{X} \in \Omega_0$, with $\mathbf{X} = X_a\mathbf{E}_a$ are the reference configuration and position of a particle in it, respectively, at a time $t = 0$. The configuration at t is defined through region Ω and particle position $\mathbf{x} \in \Omega$, with $\mathbf{x} = x_a\mathbf{e}_a$. The motion $\boldsymbol{\chi}$ can be described as a mapping of $\mathbf{X}$ to $\mathbf{x}$ in

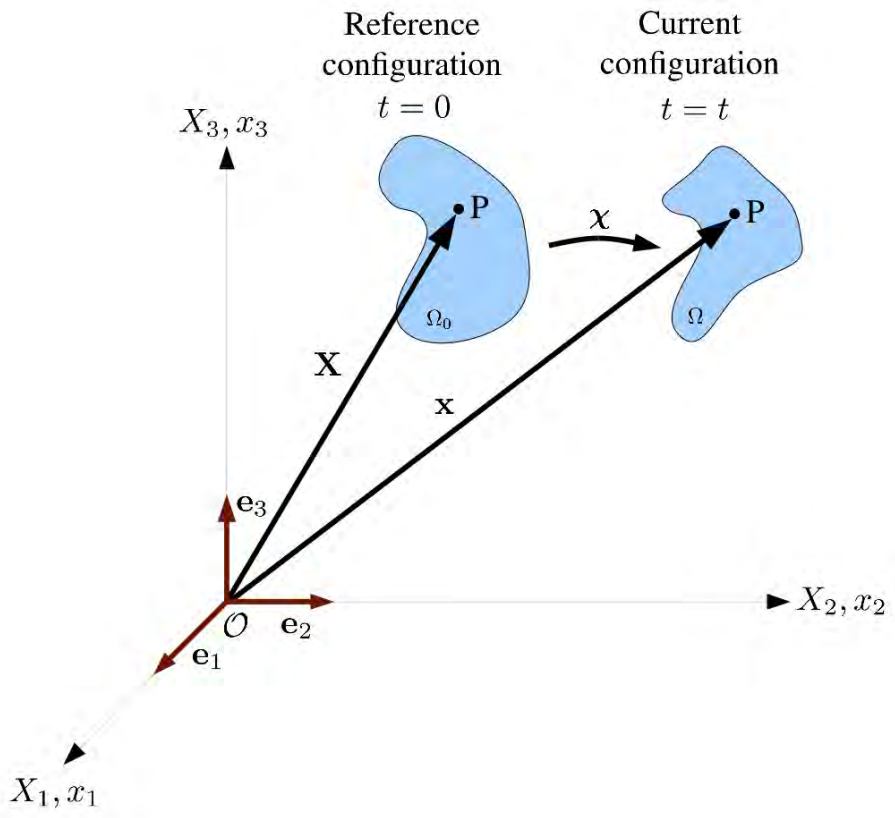

Figure 2.18: Motion of a continuum body.

known regions. Thus,

$$\boldsymbol{\chi} : \mathbf{X} \rightarrow \mathbf{x} = \boldsymbol{\chi}(\mathbf{X}, t), \qquad x_a = \chi_a(X_1, X_2, X_3, t) \tag{2.2}$$

describes a trajectory when a particle moves from $\mathbf{X}$ to $\mathbf{x}$. The motion is assumed to be invertible, so that

$$\mathbf{X} = \boldsymbol{\chi}^{-1}(\mathbf{x}, t), \qquad X_A = \chi_A^{-1}(x_1, x_2, x_3, t) \tag{2.3}$$

describes the movement of points from Ω to the reference configuration Ω_0.
The body can be changed in position (translation), orientation (rotation) and shape (deformation). The combination of translation and rotation is called rigid body motion and is time dependent. A change in shape, which means the body is deformed, is assumed to be time independent.

Deformation gradient F

In the previous section the movement of single particles of a body was described, now the deformation of curves and tangent vectors should be considered.
As shown in Figure 2.19, the material (or undeformed) curve $\mathbf{X} = \mathbf{\Gamma}(\xi)$ with $X_A = \Gamma_A(\xi)$ is a subset of Ω_0 ($\mathbf{X} \subset \Omega_0$), with ξ as parameters and $\mathbf{X}$ is associated with the reference configuration of the continuum body. If a motion $\boldsymbol{\chi}$ is subject to the body which deforms

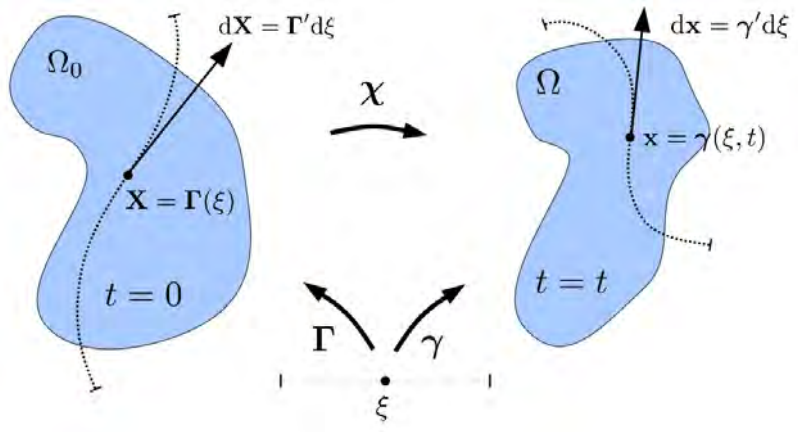

Figure 2.19: Deformation of a material curve $\mathbf{\Gamma} \subset \Omega_0$ into a spatial curve $\boldsymbol{\gamma} \subset \Omega$ as in Holzapfel (2000).

the material curve, the configuration at a time t can be described as a spatial (deformed) curve $\mathbf{x} = \boldsymbol{\gamma}(\xi, t) \subset \Omega$, $(x_a = \gamma_a(\xi, t))$.
The parametric equation at a fixed time t can be written as:

$$\mathbf{x} = \boldsymbol{\gamma}(\xi, t) = \boldsymbol{\chi}(\mathbf{\Gamma}(\xi), t), \qquad \text{or} \qquad x_a = \gamma_a(\xi, t) = \chi_a(\Gamma_A(\xi), t). \tag{2.4}$$

The tangent vectors of the curves are denoted as $\mathrm{d}\mathbf{x}$ (deformed) and $\mathrm{d}\mathbf{X}$ (undeformed). They are defined by:

$$\mathrm{d}\mathbf{x} = \frac{\partial \boldsymbol{\gamma}(\xi, t)}{\partial \xi}\mathrm{d}\xi, \quad \mathrm{d}\mathbf{X} = \frac{\partial \mathbf{\Gamma}(\xi, t)}{\partial \xi}\mathrm{d}\xi. \tag{2.5}$$

Using equation (2.4), $\mathbf{X} = \mathbf{\Gamma}(\xi)$ and then the chain rule, on equation (2.5), it can be rewritten as:

$$\mathrm{d}\mathbf{x} = \frac{\partial \boldsymbol{\chi}(\mathbf{X}, t)}{\partial \xi}\mathrm{d}\xi = \frac{\partial \boldsymbol{\chi}(\mathbf{X}, t)}{\partial \mathbf{X}}\frac{\partial \mathbf{X}}{\partial \xi}\mathrm{d}\xi = \frac{\partial \boldsymbol{\chi}(\mathbf{X}, t)}{\partial \mathbf{X}}\frac{\partial \mathbf{\Gamma}(\xi)}{\partial \xi}\mathrm{d}\xi. \tag{2.6}$$

With the definition of the deformation gradient as:

$$\mathbf{F}(\mathbf{X},t) = \frac{\partial \boldsymbol{\chi}(\mathbf{X},t)}{\partial \mathbf{X}} = \mathrm{Grad}\mathbf{x}(\mathbf{X},t), \tag{2.7}$$

and equation (2.5) it can be deduced that equation (2.6) takes the form:

$$\mathrm{d}\mathbf{x} = \mathbf{F}(\mathbf{X},t)\mathrm{d}\mathbf{X}. \tag{2.8}$$

The deformation gradient $\mathbf{F}$ has nine components for a three-dimensional problem, and it describes the behavior of motion in the neighborhood of a point. With $\mathbf{F}$, material tangent vectors can be mapped into spatial tangent vectors.
As mentioned in Section 2.5.1, we assumed that an inverse of the motion $\boldsymbol{\chi}^{-1}$ exists, therefore the inverse of the deformation gradient results in:

$$\mathbf{F}^{-1}(\mathbf{x},t) = \frac{\partial \boldsymbol{\chi}^{-1}(\mathbf{x},t)}{\partial \mathbf{x}} = \mathrm{grad}\mathbf{X}(\mathbf{x},t), \tag{2.9}$$

and it is possible to transform a deformed configuration back to the reference configuration with the rule $\mathrm{d}\mathbf{X} = \mathbf{F}^{-1}(\mathbf{x},t)\mathrm{d}\mathbf{x}$. If the body is not moved (deformed), than the deformation gradient is equal to the identity matrix ($\mathbf{F} = \mathbf{I}$) and the reference configuration has the same spacial coordinates as the configuration at the time t ($\mathbf{x} = \mathbf{X}$).
The local volume ratio $J(\mathbf{X})$ (Jacobian determinant) is defined as:

$$J(\mathbf{X}) = \mathrm{det}\mathbf{F}(\mathbf{X}) > 0, \tag{2.10}$$

and $J(\mathbf{X}) = 1$, if the material is incompressible. Which means that the motion is isochoric or volume-preserving.

Deformation of the specimen during the sample preparation

If we take all previous descriptions into account we can formulate a deformation gradient which can be used in the data analysis of our experiments (an example is given later in this section for mapping the measured angles from the stretched configuration back to the reference configuration). The reference configuration is in our case the unloaded specimen after it was cut from the artery. The deformation $\boldsymbol{\chi}$ (now, we assume no time dependency) occurs during the stretching of the specimen in all three directions of space. Any shear deformation caused by loading the specimen with the force needed to stretch it, is neglected.

Due to fixation in the aluminum frame, we also pay no attention to isotropic shrinking of the specimen, which could occur during the histological processing. Therefore, the relation between the reference configuration and the stretched configuration can be written as

$$x_x = \lambda_x X_x, \tag{2.11}$$
$$x_y = \lambda_y X_y, \tag{2.12}$$
$$x_z = \lambda_z X_z, \tag{2.13}$$

with λ_x, λ_y, λ_z representing the stretch ratios in the x-, y- and z-directions (Figure 2.1). Due to the assumption that the arterial wall is incompressible, the relation between the stretch ratios becomes

$$\lambda_x \lambda_y \lambda_z = 1, \tag{2.14}$$

denoted as incompressibility condition. With this assumption the deformation in z-direction can be written as $\lambda_z = {}^1\!/_{\lambda_x \lambda_y}$. Using equations (2.7) and (2.11) – (2.13) the deformation gradient takes on the form:

$$\left[\mathbf{F}\right] = \begin{bmatrix} \lambda_x & 0 & 0 \\ 0 & \lambda_y & 0 \\ 0 & 0 & \lambda_z \end{bmatrix}, \text{ with its inverse } \left[\mathbf{F}^{-1}\right] = \begin{bmatrix} {}^1\!/_{\lambda_x} & 0 & 0 \\ 0 & {}^1\!/_{\lambda_y} & 0 \\ 0 & 0 & {}^1\!/_{\lambda_z} \end{bmatrix}. \tag{2.15}$$

Applying the incompressibility condition on the deformation gradient $\mathbf{F}$ we can deduce the final form given by:

$$\left[\mathbf{F}\right] = \begin{bmatrix} \lambda_x & 0 & 0 \\ 0 & \lambda_y & 0 \\ 0 & 0 & (\lambda_x \lambda_y)^{-1} \end{bmatrix}, \text{ with its inverse } \left[\mathbf{F}^{-1}\right] = \begin{bmatrix} \lambda_x^{-1} & 0 & 0 \\ 0 & \lambda_y^{-1} & 0 \\ 0 & 0 & \lambda_x \lambda_y \end{bmatrix}. \tag{2.16}$$

Fiber in a continuum

We assume that the collagen fibers are embedded in a continuum and the orientation of the fiber is defined by preferred direction $\mathbf{a_0}$ and $\mathbf{a}$, for the reference and spatial configuration, respectively. The motion $\boldsymbol{\chi}$ maps the fiber orientation into the current configuration, yielding $\mathbf{a} = \mathbf{F}\mathbf{a}_0$.

The vector $\mathbf{a}$ is defined by the measured azimuthal (φ) and elevation (ϑ) angle (Figure 2.1):

$$\left[\mathbf{a}\right] = \begin{bmatrix} x \\ y \\ z \end{bmatrix} = \begin{bmatrix} \sin\vartheta\cos\varphi \\ \sin\vartheta\sin\varphi \\ \cos\vartheta \end{bmatrix}. \tag{2.17}$$

Using the inverse deformation gradient the reference configuration can be calculated:

$$\left[\mathbf{a}_0\right] = \begin{bmatrix} X \\ Y \\ Z \end{bmatrix} = \left[\mathbf{F}^{-1}\right]\left[\mathbf{a}\right]. \tag{2.18}$$

To obtain the fiber angles Θ (elevation) and Φ (azimuthal) of the reference configuration the following relations were used:

$$\Theta = \arctan\sqrt{\frac{X^2+Y^2}{Z}}, \quad \Phi = \arctan\left(\frac{Y}{X}\right). \tag{2.19}$$

Example

In the constitutive model the data needs to be present in the unloaded, undeformed configuration. Therefore, the concept of the deformation gradient, introduced earlier, is applied to obtain the angles in the undeformed specimen. A short example should demonstrate the calculation of the angles with the deformation gradient.
The azimuthal angles were measured with respect to the circumferential axis of the aorta (x-direction of the specimen, Figure 2.1). The specimen AS44 had the dimensions $6.81 \times 6.76\,\mathrm{mm}$ (distance between the markes) before the stretching and chemical fixation. Afterwards, the dimensions changed to $8.57 \times 7.81\,\mathrm{mm}$. For the histological process we assume that the dimensions did not undergo any changes because of the fixation in the aluminum frame (Figure 2.7). This yields the stretch ratios:

$$\lambda_x = \frac{x}{X} = 1.258, \quad \lambda_y = \frac{y}{Y} = 1.155 \quad \text{and} \quad \lambda_z = \frac{1}{\lambda_x\lambda_y} = 0.688. \tag{2.20}$$

As described in equation (2.16) the deformation gradient $\mathbf{F}$ has the form:

$$\left[\mathbf{F}\right] = \begin{bmatrix} \lambda_x & 0 & 0 \\ 0 & \lambda_y & 0 \\ 0 & 0 & (\lambda_x \lambda_y)^{-1} \end{bmatrix} = \begin{bmatrix} 1.258 & 0 & 0 \\ 0 & 1.155 & 0 \\ 0 & 0 & 0.688 \end{bmatrix}. \tag{2.21}$$

The calculation of the angles in the reference configuration requires the inverse of $\mathbf{F}$, which is:

$$\left[\mathbf{F}^{-1}\right] = \begin{bmatrix} 0.795 & 0 & 0 \\ 0 & 0.867 & 0 \\ 0 & 0 & 1.453 \end{bmatrix}. \tag{2.22}$$

The experimentally measured angle is described as a vector (2.17), with $\vartheta = 5.59°$ and $\varphi = 40°$ it yields

$$\begin{bmatrix} x \\ y \\ z \end{bmatrix} = \begin{bmatrix} \sin\vartheta\cos\varphi \\ \sin\vartheta\sin\varphi \\ \cos\vartheta \end{bmatrix} = \begin{bmatrix} 0.0746 \\ 0.0626 \\ 0.9952 \end{bmatrix}, \tag{2.23}$$

and can be transformed in the reference configuration by multiplication with the inverse of $\mathbf{F}$:

$$\begin{bmatrix} X \\ Y \\ Z \end{bmatrix} = \left[\mathbf{F}^{-1}\right] \begin{bmatrix} y \\ x \\ z \end{bmatrix} = \begin{bmatrix} 0.059 \\ 0.054 \\ 1.446 \end{bmatrix}. \tag{2.24}$$

The elevation angle Θ and azimuthal angle Φ of the reference configuration can be calculated as:

$$\Theta = \arctan\frac{\sqrt{X^2 + Y^2}}{Z} = 3.177°, \quad \text{and} \tag{2.25}$$

$$\Phi = \arctan\left(\frac{Y}{X}\right) = 42.425°. \tag{2.26}$$

After the transformation of all measured angles into the reference configuration, we plotted the distribution of angles with a five degree resolution, in the range of $-90°$ to $90°$ for the azimuthal Φ and elevation angle Θ. The plot yields the density of the data, which is denoted as $\rho_{\mathrm{m}}(\Theta, \Phi)$. By fitting the experimental data with, e.g., a π-periodic *von Mises* distribution, a density function can be approximated (Gasser et al. 2006). For a representative example of plotted angles for two fiber-families see Figure 2.20.

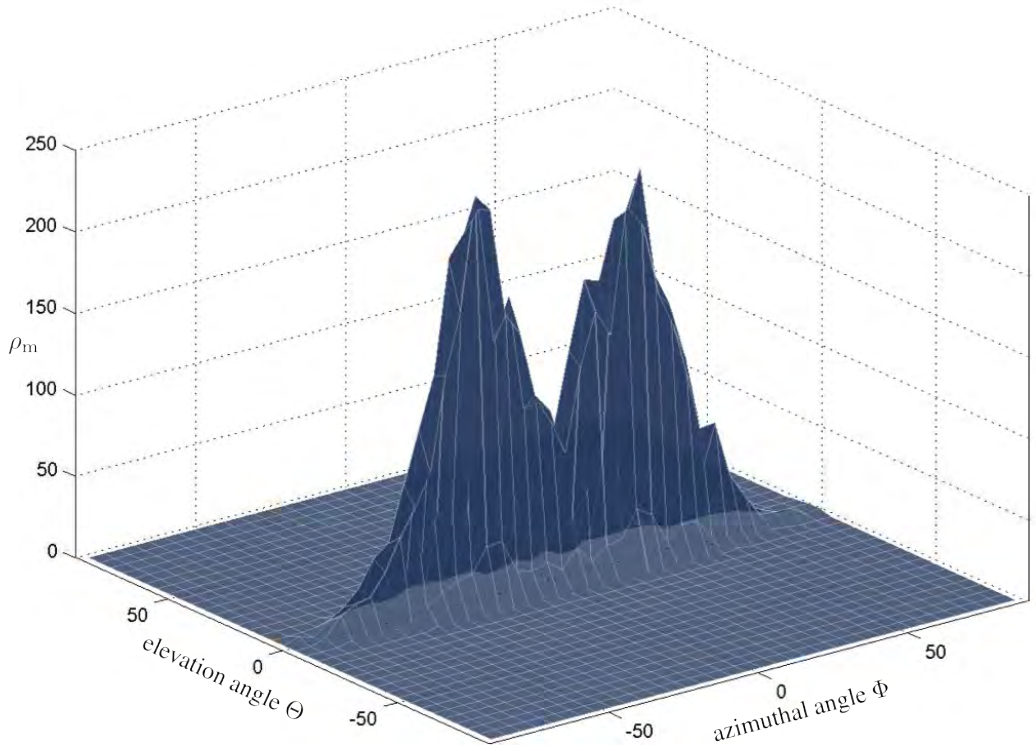

Figure 2.20: Representative three-dimensional plot of measured angles, revealing two fiber families, after transformation to reference configuration. ρ_{m} ... angle density.

2.5.2 Constitutive model

For sake of completion we mention that Gasser et al. (2006) introduced a generalized structure tensor $\mathbf{H}$ to describe the distribution of collagen fiber orientation:

$$\mathbf{H} = \kappa\mathbf{I} + (1 - 3\kappa)\mathbf{a}_0 \otimes \mathbf{a}_0, \tag{2.27}$$

were $\mathbf{I}$ is the identity tensor and $\kappa = \frac{1}{4}\int_0^{\pi} \rho(\Theta)\sin^3\Theta \mathrm{d}\Theta$. Thus, $\mathbf{H}$ depends only on a single dispersion or structure parameter κ, which represents the fiber distribution in an integral sense and describes its degree of anisotropy.

It is assumed that the embedded collagen fibers are distributed according to a transversely isotropic and π-periodic *von Mises* distribution. The dispersion parameter κ is obtained by fitting the density of the experimental data with the *von Mises* distribution. For details on this section we would like to refer the readers to Gasser et al. (2006).

3 Results

3.1 Angle measurements

From eleven aortas we measured more than 37.000 collagen fiber angles from approximately 200 histological sections at the arterial locations T1 to CI (Figure 2.2).
The mean location-specific angle values for T1 – T3 and A1 – A3 of each subject showed no significant deviation, therefore we combined them to T for the descending thoracic aorta and A for the abdominal aorta. Table 3.1 shows the results of the number of fiber families, mean elevation and azimuthal angle with corresponding standard deviations, for aortic locations T, A and CI for each layer. The prefix '$\pm$' for the azimuthal angles denotes a symmetric two fiber family collagen orientation around the circumferential axis ($\varphi = 0°$).

	Location	No. of fiber families	Φ	*SD*	Θ	*SD*
Intima	T	2 – 4	± 39	17	0	6
	A	2 – 4	± 31	18	0	6
	CI	2 – 3	± 35	18	0	6
Media	T	2	± 25	15	0	6
	A	2	± 22	15	0	5
	CI	1	0	20	0	5
Adventitia	T	2	± 55	17	0	5
	A	2	± 54	19	0	6
	CI	2	± 56	18	0	5

Table 3.1: Layer- and location-specific angle results from all eleven subjects. T...thoracic aorta, A...abdominal aorta and CI...common iliac artery, as specified in Figure 1.2. The angles Φ and Θ represent the azimuthal and the elevation angle (in degrees), respectively, as specified in Figure 2.1. *SD* are the dedicated standard deviations of the angles, $\pm$ denotes the presence of two symmetrically arranged fiber families.

3.1.1 Elevation angles Θ

The measurements of the elevation angles from the cross section images yielded in-plane (x – z plane) orientations for all fibers at all locations. No layer-specific dependencies and no significant deviations from the $x-y$ plane (Figure 2.1) could be measured, yielding $\Theta = 0°$ with a standard deviation between $5°$ and $6°$ (Table 3.1). Figure 3.1 shows a representative image of a cross section from an abdominal aorta, showing the in-plane fiber orientations.

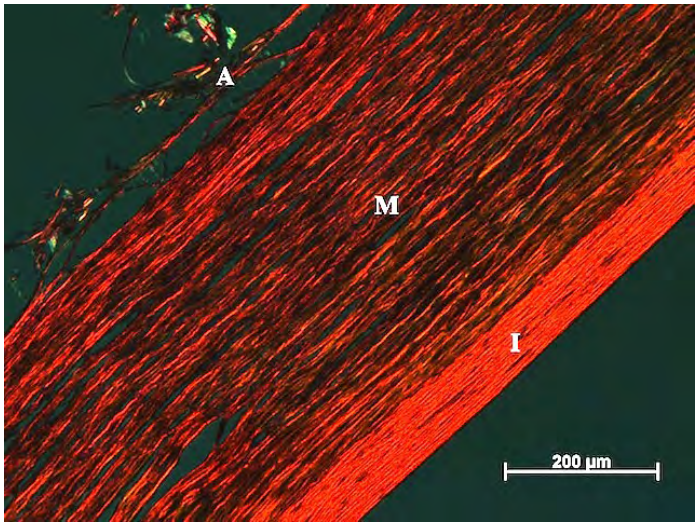

Figure 3.1: Representative image of a cross section (x – z plane) from an abdominal aorta, showing the in-plane orientations of the collagen fibers. A . . . Adventitia, M . . . Media, I . . . Intima.

3.1.2 Azimuthal angles Φ

A graphical overview of all measured layer-specific azimuthal collagen fiber angles (in the reference configuration) is provided in Figure 3.2. As can be seen, with the exception of for the media of the common iliac artery, we always observed two prominent fiber families.

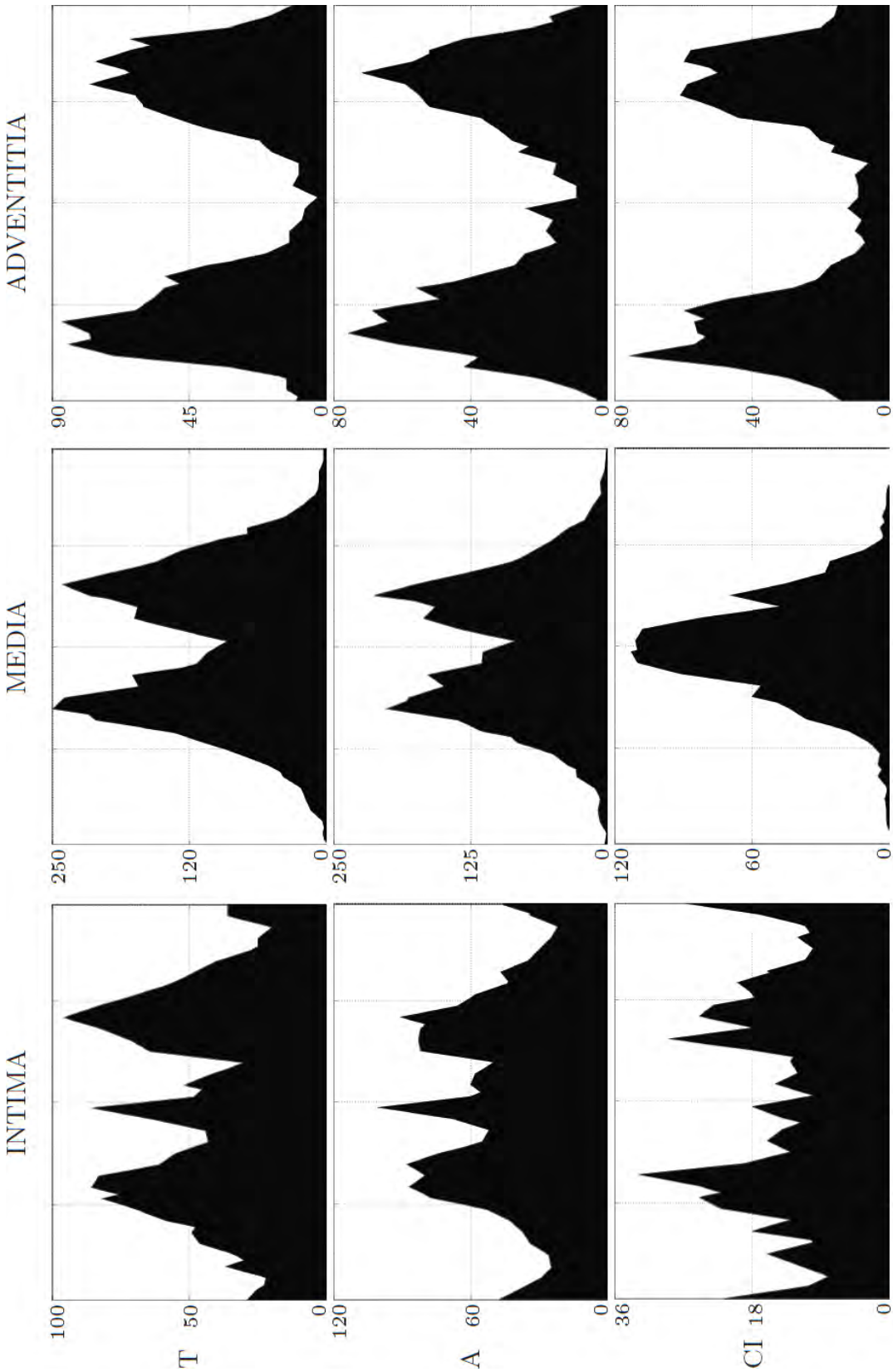

Figure 3.2: Layer-specific overview of all measured collagen fiber angles for the azimuthal angle Φ, transformed to the reference configuration.

Intima

A representative image of two main collagen fiber families is shown in Figure 3.3.

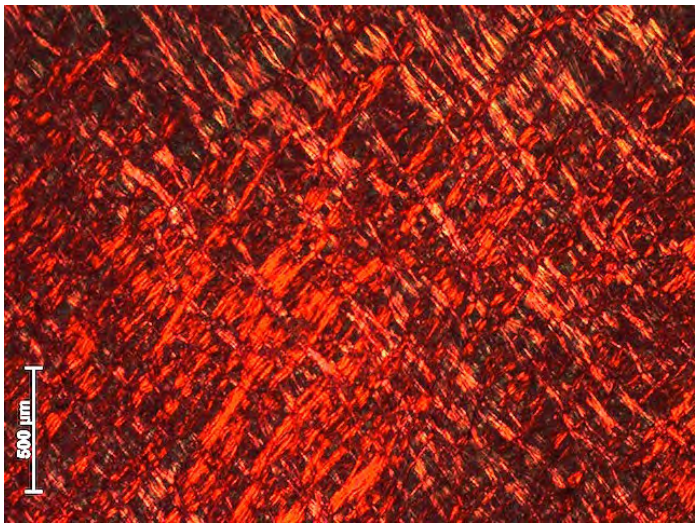

Figure 3.3: Representative image of two main fiber families in the intima.

From thoracic aortas (T1-T3) 4201 measurements were made, yielding three distinct fiber families. The first is oriented in circumferential direction ($0°$), and the others for the angles $\pm 39° \pm 18°$. Also a smaller fourth peak is visible at $90°$, which indicates a smaller amount of fibers in the axial direction.
Fiber families for the abdominal aorta (A1-A3) show similar orientations, only the symmetrical peaks were at $\pm 31° \pm 18°$, and therefore more in circumferential direction than in the thoracic aorta. 4475 measurements were taken into account.
For the common iliac artery (CI) 1254 measurements were taken and the peaks are not that clearly distinguishable. The prominent peaks are at $\pm 35° \pm 18°$.

Media

In the media two collagen fiber families were present in the thoracic and abdominal aorta (Figure 3.2, 3.4a), which were oriented more circumferentially than the collagen fibers in the intima. The mean values of the peaks are at $\pm 25° \pm 15°$ and $\pm 22° \pm 15°$ for the descending thoracic and abdominal aorta, respectively.
Interestingly, for the common iliac artery the measurements showed that the fibers are aligned in the circumferential direction $0° \pm 20°$ (Figure 3.4b) and therefore only one fiber family is present (Figure 3.2, Table 3.1). The total number of measurements were 8015,

6195 and 2453 for the descending thoracic and abdominal aorta and the common iliac artery, respectively.

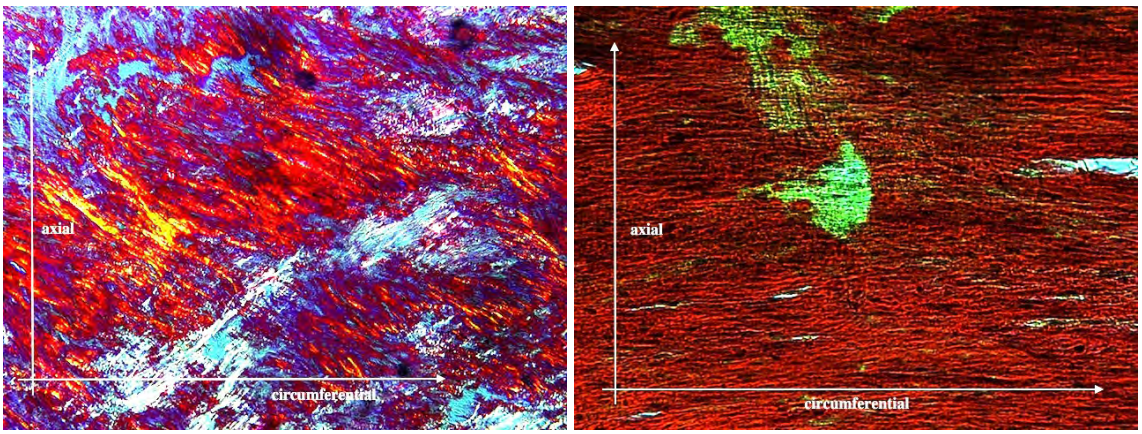

(a) **(b)**

Figure 3.4: (a) Media in a thoracic aorta with two fiber families present. (b) Media in a common iliac artery. Only one fiber family is present in circumferential direction.

Adventitia

The adventitia showed a nearly identical fiber distribution along the whole aortic tree (from T1-CI). The mean fiber angles were $\pm 55° \pm 17°$, $\pm 54° \pm 19°$ and $\pm 56° \pm 18°$ for the thoracic and abdominal aorta and common iliac artery, respectively (Figure 3.2, Table 3.1). Therefore, all examined arteries clearly showed two distinct fiber families (Figure 3.5). We measured 3194, 2809 and 2507 angles for the thoracic, abdominal and common iliac artery, respectively.

The varying number of measured azimuthal angles Φ for the thoracic and abdominal aortas and the common iliac arteries is due to different sample thicknesses, yielding varying numbers of histological sections.

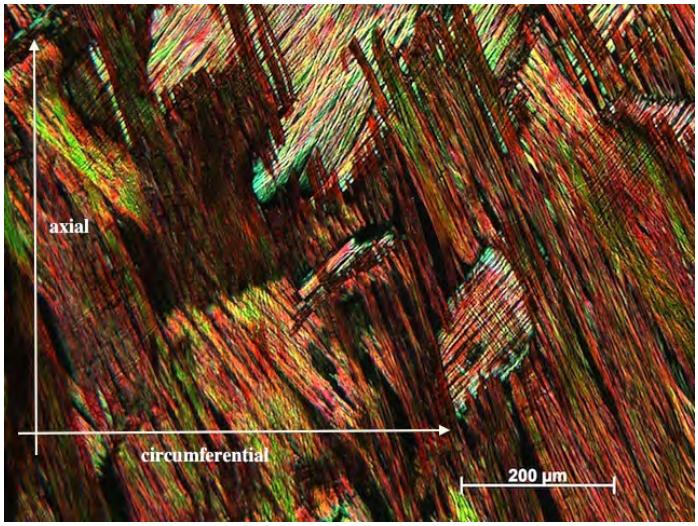

Figure 3.5: Representative image of two fiber families in the adventitia (x – y plane).

3.2 Thickness measurements

We measured the thickness of specimens at three different stages during the preparation phase: (i) undeformed, (ii) deformed after chemical fixation, (iii) after histological processing. We used at (i) an accurately calibrated video-extensometer, at (ii) a standard outside micrometer gauge and at the final stage (iii) an optical microscope.
Mean values of the total wall thickness for the descending thoracic and abdominal aorta and common iliac artery are shown in Table 3.2. At stage (i) they are $2.30 \pm 0.38\,\mathrm{mm}$, $1.79 \pm 0.30\,\mathrm{mm}$ and $1.40 \pm 0.23\,\mathrm{mm}$ for T, A and CI. The mean wall thicknesses at stage (ii) (the deformed and chemically fixed state) for the thoracic and abdominal aorta and common iliac artery are $1.41 \pm 0.23\,\mathrm{mm}$, $1.26 \pm 0.09\,\mathrm{mm}$ and $1.00 \pm 0.12\,\mathrm{mm}$, respectively. At the final stage (iii) the results are $1.39 \pm 0.18\,\mathrm{mm}$, $1.39 \pm 0.16\,\mathrm{mm}$ and $1.05 \pm 0.15\,\mathrm{mm}$ for the thoracic and abdominal aortic wall and common iliac artery wall, respectively.

Figure 3.6 shows the wall thickness as a function of age for our limited number of eleven subjects. In Table 3.3 the intima to media and the intima to media to adventitia ratio is displayed. We choose not to present the absolute layer-specific thickness values, because they could be misleading due to the non-uniformity of the arterial wall (Stary et al. 1992). In Figure 3.7 the layer-specific arterial wall thicknesses from locations T1 to A3 are presented. The much thinner common iliac arteries were not taken into account, because their values would distort the linear regressions.

Location	Video-extensometer (mm)	Micrometer gauge (mm)	Microscope (mm)
T	2.30 ± 0.38	1.41 ± 0.23	1.39 ± 0.18
A	1.79 ± 0.30	1.26 ± 0.09	1.39 ± 0.16
CI	1.40 ± 0.23	1.00 ± 0.12	1.05 ± 0.15

Table 3.2: Mean location-specific thicknesses of the total arterial wall obtained with different measurement methods applied at three different preparation phases: (i) Reference configuration, Video-extensometer; (ii) Stretched and fixed configuration, Micrometer gauge; (iii) After histological processing, Microscope. Locations: T . . . thoracic, A . . . abdominal, CI . . . common iliac.

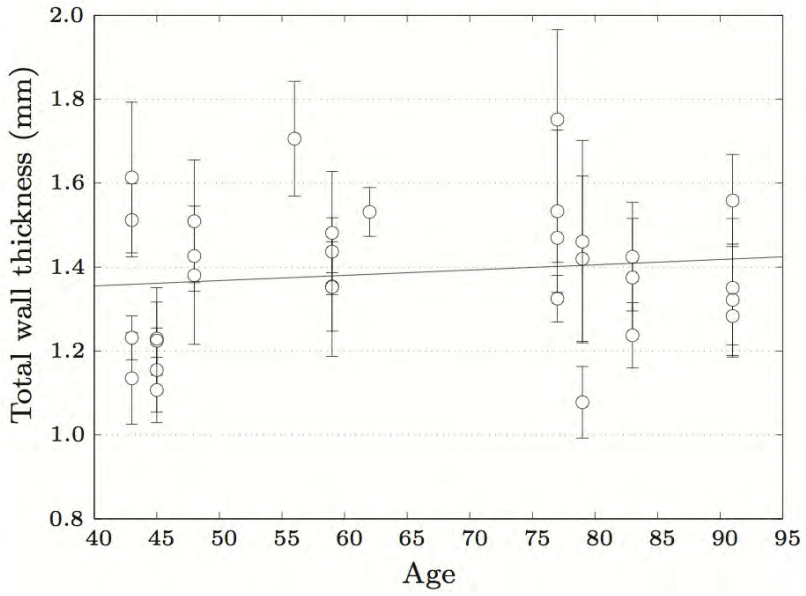

Figure 3.6: Total wall thicknesses as a function of age for eleven subjects.

Location	Intima / Media [%]	Intima / Media / Adventitia [%]
T1	21 / 79	12 / 57 / 31
T2	20 / 80	12 / 61 / 26
T3	20 / 80	10 / 52 / 38
A1	27 / 73	14 / 52 / 33
A2	41 / 59	20 / 48 / 32
A3	29 / 71	14 / 49 / 36
CI	33 / 67	14 / 44 / 42

Table 3.3: Overview of the proportional thickness overview of the single aortic layers for locations T1 – CI.

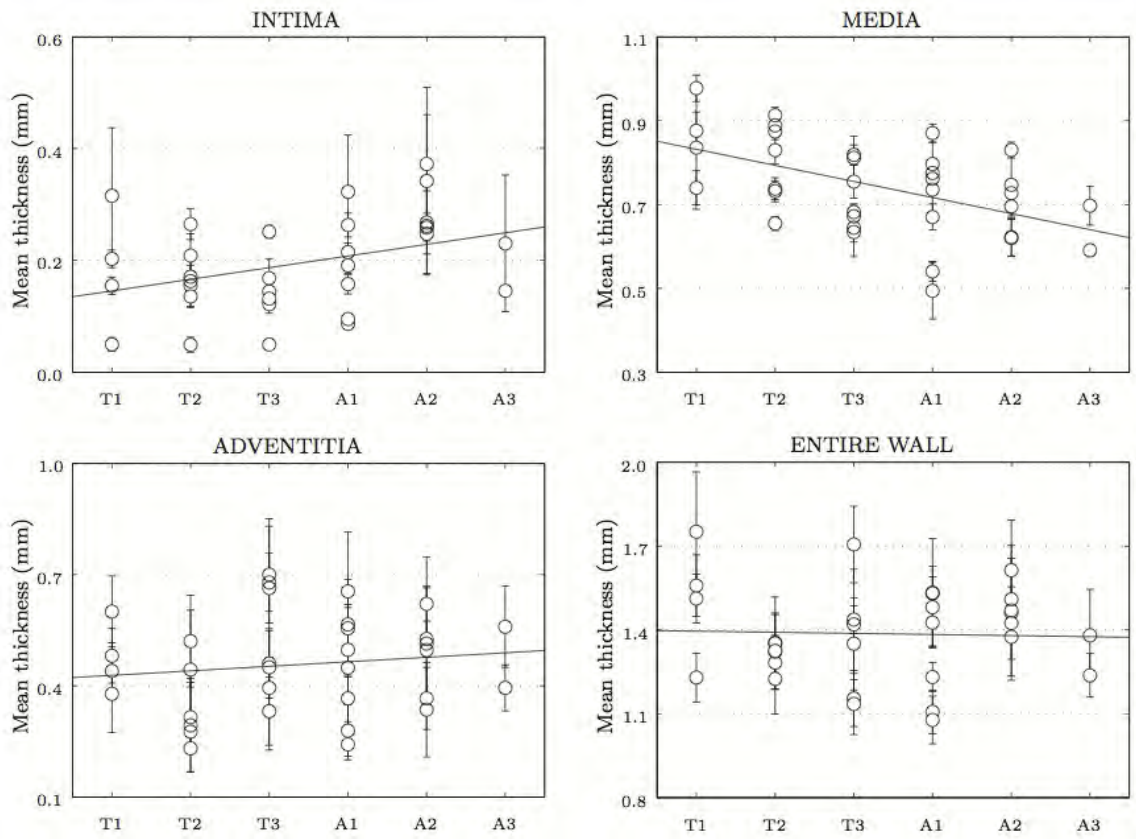

Figure 3.7: Layer-specific arterial wall thicknesses from T1 to A3. To avoid distortions of the linear regressions, the data for the much thinner common iliac arteries were not taken into account.

4 Discussion

Collagen is mechanically the most important component in many biological tissues which need withstanding uniaxial or biaxial loading, as e.g., tendons, skin, pericardium, heart valves, and arteries (Canham et al. 1996). Many publications discuss the importance of the three-dimensional collagen fiber orientation with respect to the mechanical properties of arterial walls (Canham et al. 1996, Gasser et al. 2006, Holzapfel et al. 2000, Holzapfel and Ogden 2010). To obtain different mechanical and geometrical parameters various approaches were taken, e.g., uniaxial tensile testing (Holzapfel et al. 2004, 2005), inflation testing (Humphrey et al. 1993), biaxial mechanical testing (Debes and Fung 1995, Sacks 2000), and measurements using imaging methods like ultrasound (Ahlgren et al. 1997, Pignoli et al. 1986) or MRT (Li et al. 2004). To our knowledge we measured for the first time the collagen fiber orientations in healthy human descending aortas and common iliac arteries with non-atherosclerotic thickening of the intima. Most data in the literature originates from smaller human arteries (Finlay et al. 1995, Smith et al. 1981) or animal arteries (Wicker et al. 2008), which can not be assumed to be the same in human aortic tissue (Wolinsky and Glagov 1964).

4.1 Angle measurements

Over 37.000 fiber angles from the descending aorta and common iliac arteries were experimentally measured and analyzed, which is a significantly larger number compared to other studies (Finlay et al. 1995, Wicker et al. 2008). Our results yield layer-specific collagen fiber families for the azimuthal angle Φ, which differ in angle distribution and dispersion for different parts of the aorta and common iliac artery.
The measurement results for the elevation angle Θ manifest no layer- nor location-specific dependencies. The collagen fibers are arranged in-plane with the arterial wall yielding a mean elevation angle $\Theta = 0^\circ \pm 5.5^\circ$ (Table 3.1).

For the different arterial wall layers in the descending thoracic and abdominal aorta we observed two symmetric fiber families for the mean azimuthal angle Φ. The collagen fiber families showed a slightly circumferential preference in the intima ($\pm 35^\circ \pm 18^\circ$) a nearly circumferential orientation in the media ($\pm 23.5^\circ \pm 15^\circ$) and a most axial orientation in the adventitia ($\pm 54.5^\circ \pm 18^\circ$) as shown in Table 3.1. These results correspond with measured mechanical properties of uniaxial tensile stress-stretch responses reported by Holzapfel et al. (2004, 2005), where the media and adventitia showed a stiffer behavior in circumferential and in axial direction, respectively. Hence a variation of Φ between the arterial layers was expected, and this layer-specific dependency of Φ is exactly what we observed and can be expressed through the differences between the angles of the fiber families: $\Delta\Phi_{\mathrm{MI}} = 11.5^\circ$ (media – intima) and $\Delta\Phi_{\mathrm{MA}} = 31^\circ$ (media – adventitia).
The layer-specific collagen fiber families for the common iliac artery were nearly the same as for the descending aorta with the exception of the media. While in the descending aorta two fiber families are present, the media in the common iliac artery showed one fiber family highly alignment in the circumferential direction at $0^\circ \pm 20$ (Figure 3.4b). This is assumed to be related to the different function of common iliac arteries versus the aorta. Wicker et al. (2008) and Finlay et al. (1995) reported the same highly circumferential alignment for collagen fibers in brain arteries. These fibers suppress extension and ensure constant blood pressure in the brain, whereas the elastic aorta needs to absorb pulsating pressure waves originating from the heart. Helical oriented collagen fibers allow for small circumferential extensions of the aortic tube, but prevent an over-stretching of the vessel wall caused by e.g., high blood pressure when exercising.
The results for the intima showed not only two fiber families symmetrically arranged between the major axes, but also one in axial and one in circumferential direction (Table 3.1, Figure 2.14). However, the fibers in axial and circumferential direction were not present in every measured tissue sample.
Our results for the azimuthal collagen fiber angles in the adventitia correlate with findings of Finlay et al. (1995), who reported one fiber family at 53° for human cerebral arteries.

4.2 Thickness measurements

We measured the thickness of aortic wall samples at three different stages during the preparation phase: (i) undeformed sample, (ii) deformed after chemical fixation, (iii) after histological processing.

For (i) a video-extensometer was used and, although the video-extensometer is very accurate when correctly calibrated, the measurements can be challenging. In some samples deposits, plaque and calcifications are present, and generally wall thicknesses are naturally not uniform (Stary et al. 1992).
Our measurements with the video-extensometer at stage (i) for the thoracic and abdominal aorta and common iliac artery the mean wall thicknesses were $2.30 \pm 0.38\,\mathrm{mm}$, $1.79 \pm 0.30\,\mathrm{mm}$ and $1.40 \pm 0.23\,\mathrm{mm}$, respectively (Table 3.2). The mean wall thicknesses Labrosse et al. (2009) measured for the thoracic and abdominal aorta were $1.56 \pm 0.14\,\mathrm{mm}$ and $1.25 \pm 0.27\,\mathrm{mm}$, respectively. For the abdominal aorta Holzapfel et al. (2007) reported wall thicknesses of:

- $1.46 \pm 0.35\,\mathrm{mm}$ for a ring (after 30min),
- $1.36 \pm 0.45\,\mathrm{mm}$ for a circumferential strip,
- $1.64 \pm 0.44\,\mathrm{mm}$ for an axial strip.

The difference of the mean values is likely to be related to the use of the whole descending aorta in our experiments (which is thicker near the heart) and due to the nearly not distinguishable appearance of the adventitia and the surrounding tissue at the preparation, which could lead to varying thickness data for the adventitia. We tried deliberately not to cut into the adventitia, which sometimes might cause surrounding tissue to be still in place and therefore enlarge measured wall thicknesses.
Our measured wall thicknesses at the unstretched state (i) correlate well with the data from a study of thoracic wall thicknesses from participants without clinical cardiovascular disease, where the means ranged from $2.11 \pm 0.06\,\mathrm{mm}$ for women to $2.32 \pm 0.06\,\mathrm{mm}$ for men (Li et al. 2004).
The measurements at state (ii) were performed with a micrometer gauge. We observed $1.41 \pm 0.23\,\mathrm{mm}$ for thoracic, $1.26 \pm 0.09\,\mathrm{mm}$ for abdominal aortic walls and $1.00 \pm 0.12\,\mathrm{mm}$ for common iliac artery walls. These data correspond well with the findings discussed above from Labrosse et al. (2009), Holzapfel et al. (2007), although our values were obtained from a stretched configuration.
The measurements of the thickness of soft tissue is not unproblematic, if methods with tissue contact are used (Lee and Langdon 1996, Humphrey 2002). In our case, measurements with a micrometer gauge was the only contact method (Section 2.4.2). Because they were performed after chemical fixation, where the tissue is hardened, the introduced error

by compressing the tissue with the micrometer gauge during the measurement should be minimal.
At the final stage (iii) the measurements were performed with an optical microscope. We observed that the media is mainly responsible for the decrease in the total wall thickness along the aortic tree, because the thickness of the intima and the adventitia remains nearly constant for all locations T1 – CI (Figure 3.7). No significant difference in total wall thickness could be seen between the thoracic and abdominal aortas.
Also individual non-atherosclerotic intimal thickening can influence the thickness of the specimen. It is assumed that intimal thickening occurs due to changes in the blood flow or wall tension and because of the branchings. These changes can result in a reduced wall shear stress or elevated tensile stress or both (Stary 1992). The intima remodels itself to withstand the changed mechanical environment. This thickening could be observed in the abdominal aorta, when analyzing the intima to media ratio (Table 3.3). While in the thoracic aorta the intima to media ratio remains constant for locations T1 – T3, a significant increase in intima thickness was found for the abdominal aorta starting at A1 around the branchings of the celiac arteries, where constant blood flow is interrupted (Table 3.3). In our case the intima to media ratios varied between 0.25 – 0.70 (calculated from our microscope measurements) and fit into the range for normal arteries (0.1 – 1.0) of humans according to guidelines from the American Heart Association (Stary et al. 1992).
For our limited number of specimens no gender dependent differences and only a small age dependency could be observed for the arterial wall thicknesses (Figure 3.6). This trend is consistent with the reported data form Stary et al. (1994), Purinya and Kas'yanov (1975). Our subjects were relatively old, the average age was 63 years, therefore we assume that a stronger age dependent thickening could be observed if younger objects (< 40 years) would be included.

The dependency of the mechanical response from the human arteries on the layer- and location-specific fiber alignment was already assumed (Holzapfel et al. 2005). Our results provide qualitative and quantitative structural data for the collagen fiber orientations of healthy non-atherosclerotic arterial walls. This data can be used directly to obtained dispersion parameters for constitutive models for arterial walls, e.g., the 'κ-model' from Gasser et al. (2006), resulting in an better determination of these parameters. Therefore, the modeling of the cardiovascular system should be improved.

4.3 Limitations

Due to a change in geometry from the cylindrical artery to a planar specimen during the sample preparation, the mean collagen fiber angles may differ slightly for the *in vivo* state. Our histological sections are discontinuous samples due to the $100\,\mu\mathrm{m}$ space we left between subsequent cuts (Figure 2.4). Therefore, we could not measure the fiber angles continuously throughout the vessel wall in radial direction. Our reported angles are mean values for each layer and independent on the radial position of the section within each layer.

Despite great precautions there is always the risk of introducing errors during the sample preparation process, due to the experimental nature of this research. Using the universal stage an accuracy of measurement of 0.5 degree was possible. We rounded the angles to whole numbers and plotted the data in a 5 degree grid to obtain the measured distribution of the fibers (Figure 2.20).

The measurements with the micrometer gauge showed slightly smaller values than the ones with the microscope, which is probably due to physical compression during the measurements.

Bibliography

Å. R. Ahlgren, F. Hansn, B. Sonesson, and T. Länne. Stiffnes and diameter of the common carotid artery and abdominal aorta in women. *Ultrasound. Med. Biol.*, 23:983–988, 1997.

K. A. Athanasiou and R. M. Natoli. *Introduction to Continuum Biomechanics*. Morgan & Claypool, 2009.

M. J. Buehler. Nanomechanics of collagen fibrils under varying cross-link densities: Atomistic and continuum studies. *J. Mech. Behav. Biomed.*, 1:59–67, 2008.

P. B. Canham, H. M. Finlay, and S. Y. Tong. Stereological analysis of the layered collagen of human intracranial aneurysms. *J. Microsc.*, 183:170–180, 1996.

J. C. Debes and Y. C. Fung. Biaxial mechanics of excised canine pulmonary arteries. *Am. J. Physiol. Heart Circ. Physiol.*, 269:H433–H442, 1995.

H. M. Finlay, L. McCullough, and P. B. Canham. Three-dimensional collagen organization of human brain arteries at different transmural pressures. *J. Vasc. Res.*, 32:301–312, 1995.

P. Fratzl. Collagen: Structure and mechanics, and introduction. In P. Fratzl, editor, *Collagen: Structure and Mechanics*, pages 1–13. Springer, 2008.

Y. C. Fung. *Biomechanics: Mechanical Properties of Living Tissues*. Springer, New York, 2nd edition, 1993.

T. C. Gasser, R. W. Ogden, and G. A. Holzapfel. Hyperelastic modelling of arterial layers with distributed collagen fibre orientations. *J. R. Soc. Interface*, pages 15–35, 2006.

R. A. Grant. Content and distribution of aortic collagen, elastin and carbohydrate in different species. *J. Atheroscler. Res.*, 7:463–472, 1967.

X. Guo and G. S. Kassab. Distribution of stress and strain along the porcine aorta and coronary arterial tree. *Am. J. Physiol. Heart Circ. Physiol.*, 286:2361–2368, 2004.

H. C. Han and Y. C. Fung. Longitudinal strain of canine and porcine aortas. *J. Biomech.*, 28:637–641, 1995.

G. A. Holzapfel. *Nonlinear Solid Mechanics: A Continuum Approach for Engineering*. John Wiley & Sons, 2000.

G. A. Holzapfel and R. W. Ogden. Constitutive modelling of arteries. *Proc. R. Soc. A.*, 466:1551–1597, 2010.

G. A. Holzapfel, T. C. Gasser, and R. W. Ogden. A new constitutive framework for arterial wall mechanics and a comparative study of material models. *J. Elasticity*, 61:1–48, 2000.

G. A. Holzapfel, G. Sommer, and P. Regitnig. Anisotropic mechanical properties of tissue components in human atherosclerotic plaques. *J. Biomech. Eng.*, 126:657–665, 2004.

G. A. Holzapfel, G. Sommer, C. T. Gasser, and P. Regitnig. Determination of layer-specific mechanical properties of human coronary arteries with nonatherosclerotic intimal thickening and related constitutive modeling. *Am. J. Physiol. Heart Circ. Physiol.*, 289: H2049–H2058, 2005.

G. A. Holzapfel, G. Sommer, M. Auer, P. Regitnig, and R. W. Ogden. Layer-specific 3D residual deformations of human aortas with non-atherosclerotic intimal thickening. *Ann. Biomed. Eng.*, 35:530–545, 2007.

J. D. Humphrey. *Cardiovascular Solid Mechanics. Cells, Tissues, and Organs*. Springer, New York, 2002.

J. D. Humphrey and P. B. Canham. Structure, mechanical properties and mechanics of itracranial saccular aneurysms. *J. Elasticity*, 61:49–81, 2000.

J. D. Humphrey, T. Kang, P. Sakarda, and M. Anjanappa. Computer-aided vascular experimentation: A new electromechanical test system. *Ann. Biomed. Eng.*, 21:33–43, 1993.

L. C. Junqueira, G. Bignolas, and R. R. Brentani. Picrosirius staining plus polarization microscopy, a specific method for collagen detection in tissue sections. *Histochem. J.*, 11:447–455, 1979.

L. C. Junqueira, G. S. Montes, and E. M. Sanchez. The influence of tissue section thickness on the study of collagen by the picosirius-polarization method. *Histochemistry*, 74:153–156, 1982.

M. R. Labrosse, C. J. Beller, T. Mesana, and J. P. Veinot. Mechanical behavior of human aortas: Experiments, material constants and 3-D finite element modeling including residual stress. *J. Biomech.*, 42:996–1004, 2009.

M. Landuyt. Structural quantification of collagen fibers in abdominal aortic aneurysms. Master's thesis, KTH Solid Mechanics, Stockholm, and Department of Civil Engineering, Gent, 2006.

G. Lang. *Histotechink: Praxislehrbuch für die Biomedizinische Analytik*. Springer, Wien, 2006.

B. M. Learoyd and M. G. Taylor. Alterations with age in the viscoelastic properties of human arterial walls. *Circ. Res.*, 18:278–292, 1966.

J. M. Lee and S. E. Langdon. Thickness measurement of soft tissue biomaterials: A comparison of five methods. *J. Biomech.*, 29:829–832, 1996.

A. E. Li, I. Kamel, F. Rando, M. Anderson, B. Kumbasar, J. A. C. Lima, and D. A. Bluemke. Using MRI to assess aortic wall thickness in the multiethnic study of atherosclerosis: Distribution by race, sex, and age. *Am. J. Roentgenol.*, 182:593–597, 2004.

M. O'Rourke. Mechanical principles in arterial disease. *Hypertension*, 26:2–9, 1995.

P. Pignoli, E. Tremoli, A. Poli, P. Oreste, and R. Paoletti. Intimal plus medial thickness of the arterial wall: A direct measurment with ultrasound imaging. *Circulation*, 74: 1399–1406, 1986.

H. Puchtler, F. S. Waldrop, and L. S. Valentine. Polarization microscopic studies of connective tissue stained with picro-sirius red FBA. *Beitr. Pathol.*, 150:174–187, 1973.

B. A. Purinya and V. A. Kas'yanov. Mechanical properties of the wall of the human abdominal aorta after endarterectomy. *Mech. Comp. Mat.*, 11:598–602, 1975.

M. S. Sacks. Biaxial mechanical evaluation of planar biological materials. *J. Elasticity*, 61:199–246, 2000.

J. F. H. Smith, P. B. Canham, and J. Starkey. Orientation of collagen in the tunica adventitia of the human cerebral artery measured with polarized light and the universal stage. *J. Ultrastruct. Res.*, 77:133–145, 1981.

H. C. Stary. Composition and classification of human atherosclerotic lesions. *Virchows Archiv A Pathol. Anat.*, 421:277–290, 1992.

H. C. Stary, D. H. Blankenhorn, A. B. Chandler, S. Glagov, W. Insull Jr., M. Richardson, M. E. Rosenfeld, S. A. Schaffer, C. J. Schwartz, W. D. Wagner, and R. W. Wissler. A definition of the intima of human arteries and of its atherosclerosis-prone regions. a report from the committee on vascular lesions of the council on arteriosclerosis, American Heart Association. *Arterioscler. Thromb. Vasc. Biol.*, 12:120–134, 1992.

H. C. Stary, A. B. Chandler, S. Glagov, W. Insull Jr., M. E. Rosenfeld, S. A. Schaffer, C. J. Schwartz, W. D. Wagner, and R. W. Wissler. A definition of initial, fatty streak, and intermediate lesions of atherosclerosis. *Circulation*, 89:2462–2478, 1994.

W. Sun, M. S. Sacks, and M. J. Scott. Effects of boundary conditions on the estimation of the planar biaxial mechanical properties of soft tissue. *J. Biomech. Eng.*, 127:709–715, 2005.

B. K. Wicker, H. P. Hutchens, Q. Wu, A. T. Yeh, and J. D. Humphrey. Normal basilar artery structure and biaxial mechanical behaviour. *Comput. Methods Biomech. Biomed. Engin.*, 11:539–551, 2008.

H. Wolinsky and S. Glagov. Structural basis for the static mechanical properties of the aortic media. *Circ. Res.*, 14:400–413, 1964.

H. Wolinsky and S. Glagov. Comparison of abdominal and thoracic aortic medial structure in mammals. deviation of man from the usual pattern. *Circ. Res.*, 25:677–686, 1969.

M. Wolman and F. H. Kasten. Polarized light microscopy in the study of the molecular structure of collagen and reticulin. *Histochemistry*, 85:41–49, 1986.

Y. E. Yarker, R. M. Aspden, and D. W. L. Hukins. Birefringence of articular cartilage and the distribution of collagen fibril orientations. *Connect. Tissue. Res.*, 11:207–213, 1983.

Statutory Declaration

I declare that I have authored this Thesis independently, that I have not used other than the declared sources/resources, and that I have explicitly marked all material, which has been quoted by the relevant reference.

date

signature